Sedimentation study of Hirakud Reservoir, Odisha using Optic and Microwave Remote Sensing Technology (NIH-16_ 2017_26)

National Hydrology Project
Department of Water Resources, River Development and Ganga Rejuvenation, Ministry of Jal Shakti, New Delhi

Department of Water Resources, Bhubaneswar, Odisha

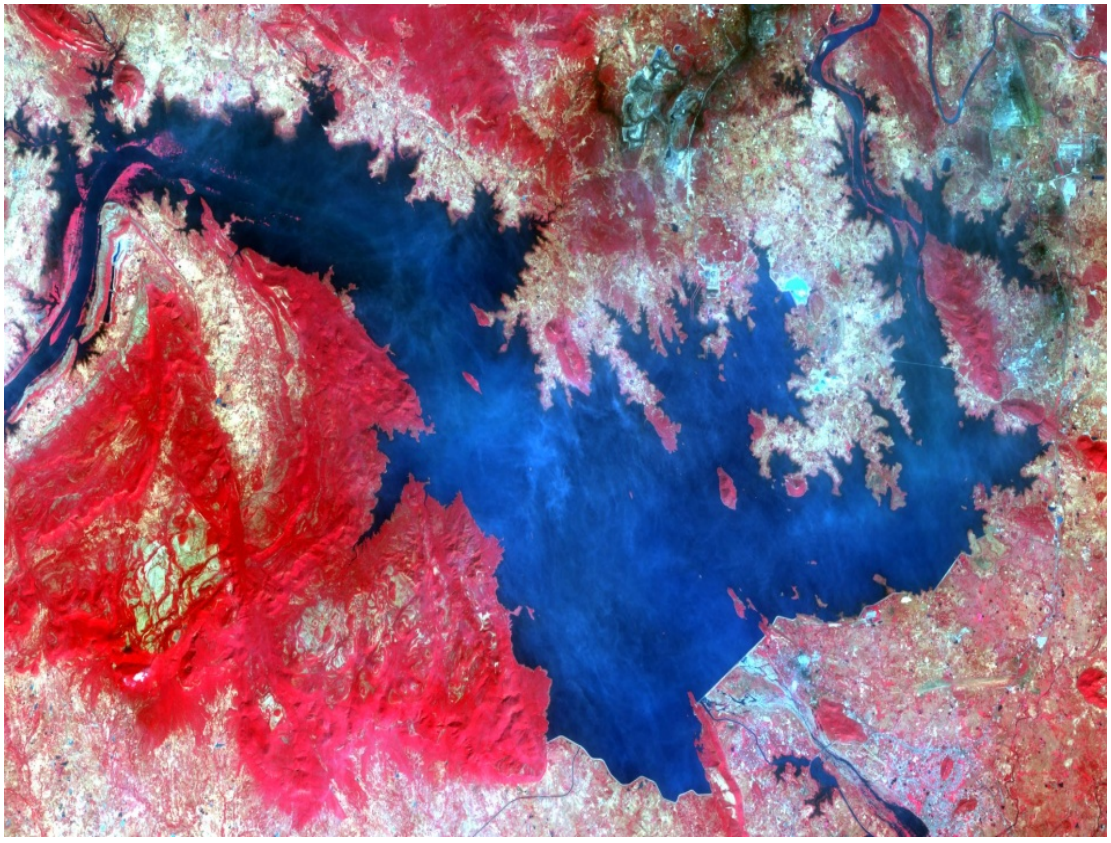

National Institute of Hydrology, Roorkee – 247 667

March, 2021

Dr.V.S.Jeyakanthan, **Scientist-E**	आपो हि ष्ठा मयोभुवः	**National Institute of Hydrology,** **Roorkee – 247 667**

PREFACE

The present study has been carried out in Hirakud reservoir. The reservoir is located in Upper Mahanadi basin in Odisha state. Efficient reservoir management calls for periodic assessment of its capacity. Capacity surveys of reservoirs are important to study patterns and rate of sedimentation for defining appropriate measures for controlling sediment inflow, for managing the available storage in the reservoir and for optimum reservoir operation schedule based on realistic assessment of available storage. Data from space platforms can play a significant role in reservoir capacity surveys. In the recent past, satellite remote sensing has emerged as an important tool in carrying out reservoir capacity surveys rapidly, frequently and economically. Multi-temporal satellite data provide information on elevation contour areas directly in the form of water spread areas. The traditional methodology involves per-pixel classification approach to delineate the water-spread. One of the limitations of the per-pixel approach is that the border pixels, containing water with soil and vegetation, are also classified entirely as water pixels, thereby giving inaccurate estimate of the water-spread area. The error induced by per-pixel classification approach can be minimized by utilizing the efficacy of the novel methodology known as the sub-pixel classification approach and super resolution mapping approach. The best methodology among per-pixel, sub-pixel and super resolution has been evaluated and identified that the super resolution approach produces less error than the other two. With the accurately estimated sedimentation in the reservoir, the dam authorities can go for suitable remedial measures and the reservoir operation schedule can be planned for optimum utilization of available water.

Odisha region is often experience cyclonic storms and severe monsoon activities in such situations optical satellite data could not fulfill it's usefulness due to coverage of clouds over the study area. To overcome this problem in this study the feasibility microwave data has been evaluated to quantify the water-spread area and in turn the rate of sedimentation of Hirakud reservoir as a second task.

The study entitled 'Sedimentation study of Hirakud Reservoir, Odisha using Optic and Microwave Remote Sensing Technology' is carried out by Dr.V.S.Jeyakanthan, Dr.J.V.Tyagi, Dr.Y.R.Satyaji Rao and Sh.R.Venkataramana of National Institute of Hydrology.

Place: Kakinada
Date

Signature
(V.S.Jeyakanthan)

Project Team	
Lead organization	Dr.V.S.Jeyakanthan, Scientist-E (PI) Dr.J.V.Tyagi, Director (Co-PI) Dr.Y.R.Satyaji Rao, Head & Sc-G (Co-PI) Sh.R.Venkataramana, Scientist-D (Co-PI) National Institute of Hydrology, Roorkee – 247 667.
Name and address of Implementing Agency	Enginer-in-Chief, Department of Water Resources, Bhubaneswar.

Document control sheet

Title	Sedimentation study of Hirakud Reservoir, Odisha using Optic and Microwave Remote Sensing Technology
PDS number	NIH-16_ 2017_26
Date of approval	November 2017
Budget in time of original approval (For Partner and for Lead)	Rs. 51.19 Lakh
Revised Budget (For Partner and for Lead)	Rs.9.77 Lakh
Date of commencement	31st August 2017
Date of completion	31st March 2021
Number of page	75
Number of figures and tables	Figures 14 and Tables 19

Abstract

Remote sensing technique provides cost- and time-effective estimation of the live capacity of a reservoir. Multi-date satellite remote sensing data provide information on elevation contours, in the form of water spread area, at different water levels of a reservoir. Till date water-spread area from the satellite data is quantified using per-pixel based approach, this approach could not classify the periphery pixels of the water-spread area properly due to mixed in nature of the border pixels and hence land in less accurate results. To eliminate this inaccuracy a sub-pixel and super-resolution based approach has been used to accurately quantify the water-spread of the Hirakud reservoir and to identify the best approach among per-pixel, sub-pixel and super resolution methodologies.

Odisha region is often experience cyclonic storms and severe monsoon activities in such situations optical satellite data could not fulfill it's usefulness due to coverage of clouds over the study area. To overcome this problem in this study it is decided to evaluate the feasibility microwave data to quantify the water-spread area and in turn the rate of sedimentation of Hirakud reservoir as a second task.

Landsat-8 and Sentinel-2 which provides frequent and high resolution data has been used between the water level 183.51 m and 191.84. Band thresholding, fraction images and the resolution enhanced images has been utilized in the per-pixel, sub-pixel and super resolution classification approaches for the estimation of water spread area (WSA). The WSA thus derived has been used to calculate the capacity and the rate of siltation in the reservoir. The estimated cumulative live storage capacity of the Hirakud reservoir, according to per-pixel, sub-pixel and super resolution approaches are 4419.60 M.cum, 4431.92 M.Cum and 4451.06 M.Cum respectively for the period 2018-19. The assessment reveals that the rate of siltation in the live storage capacity of the reservoir is 22.56, 22.39 and 22.09 M.Cum/year according to per-pixel, sub-pixel and super resolution approaches respectively. Water spread area is the only input from the satellite used for the estimation of capacity of the reservoir. Therefore the water spread area arrived using per-pixel, sub-pixel and super resolution approaches has been validated using high resolution satellite data. The validation reveals that super resolution produced less error (4.44%) than the per-pixel (5.39%) and sub-pixel (5.02%) classification approaches. This shows that the super resolution based approach can be applied to estimate the capacity of the reservoirs with higher accuracy than the per-pixel and sub-pixel based approaches.

Eleven satellite pass of microwave data (Sentinel 1-SAR) between the water level 181.79m and 190.19m was available for the period 2018-19. The pre-processing techniques were applied to all the eleven SAR, dual polarized data. From the VV and VH data thresholiding methodology was utilized to identify the water pixels. It was found that the water pixels contain values ranging from -40.62db to -21.58db, these pixels were extracted and the water spread area were estimated. The assessment revealed that the live storage capacity of the Hirakud reservoir, using microwave satellite data (Sentinel-1A) for the period 2018-19 was 4430.78 M.cum. Hence, the rate of sedimentation in the live storage capacity of Hirakud reservoir is estimated at 22.41 M.Cum/year. This shows that the amount of sediment deposited in the Hirakud reservoir is estimated at-par with optic satellite data, therefore the microwave satellite is a better replacement to the cloud covered optic data.

Originating unit	Deltaic Regional Centre, National Institute of Hydrology
Key words	Water spread area, Reservoir capacity, Per-pixel, sub-pixel, super resolution mapping, microwave satellite data
Security classification	Restricted/ Unrestricted
Distribution	Restricted

CONTENTS

LIST OF TABLES

LIST OF FIGURES

CHAPTER-1

INTRODUCTION

India is a vast country with high spatial and temporal variability of rainfall. In order to tap the available water resources and to utilize the water in accordance with the requirements, a number of river valley projects have been constructed for serving various conservation purposes, such as water supply for domestic and industrial purposes, irrigation, hydropower generation, navigation and recreation. One of the principal factors that threaten the life of such projects is the accumulation of sediments in the reservoirs. Sedimentation reduces the storage capacity of reservoirs and hence their ability to conserve water for various intended purposes. Sedimentation also reduces the survival of aquatic and restricts the use of water for multiple purposes.

Due thought is necessary towards the capacity surveys of the reservoir at the planning stage and afterwards. Periodical capacity surveys of the reservoir help in assessing the rate of sedimentation and reduction in storage capacity. Every reservoir will ultimately silt up but the useful life of the reservoir can be increased if proper remedial measures are adopted. This is not only necessary for efficient management of reservoir but also helps in taking a decision about treatment of catchment area, if the rate of sedimentation is excessive. The analysis of catchment area will help in taking various measures to reduce the entry of silt in the reservoir.

In order to determine the useful life of a reservoir it is essential to periodically conduct the surveys and assess the sedimentation rate in a reservoir. Also for proper allocation and management of water from a reservoir knowledge about the sediment deposition pattern in various zones of a reservoir is essential. With the correct knowledge of the sedimentation process going on in a reservoir, remedial measures can be undertaken well in advance and reservoir operation schedule can be planned for optimum utilization of water.

For assessing the sedimentation deposition pattern in a reservoir, systematic capacity surveys of the reservoir are conducted periodically. Present conventional techniques of sediment quantification in a reservoir, like the hydrographic surveys and inflow-outflow methods are cumbersome, expensive and time consuming. Remote sensing through its spatial, spectral and temporal attributes can provide synoptic, repetitive and timely information regarding the water spread area of the reservoir.

For the quantification of capacity of a reservoir, the only thematic information that has to be extracted from the satellite data is the water-spread area at different water levels of the reservoir. The different approaches such as maximum likelihood, minimum distance to mean classification and band threshold method, to delineate thematic information from the remote sensing digital data adopt the per-pixel based methodology and assign a pixel to a single land cover type whereas in reality, a single pixel may contain more than one land cover (known as a mixed pixel). Mixed pixels are common especially near the boundaries of two or more discrete classes. The boundary pixels of the water-spread area that are mixed in nature, representing soil, vegetation class with moisture are also classified as water pixels when a per-pixel based approach is applied, thereby producing inaccurate estimate of the water-spread area. To accurately compute the water-spread area to the maximum possible extent, thereby reducing the error in the estimation of capacity of a reservoir, a sub-pixel or linear

mixture model (LMM) and super resolution approach has been chosen for classifying the boundary pixels of water-spread area from different water levels of Hirakud reservoir located in Odisha state of India. The best methodology among the per-pixel, sub-pixel and super-resolution approaches will be identified to accurately estimate the sediment deposited in the Hirakud reservoir.

Odisha region is often experience cyclonic storms in such situations optical satellite data could not fulfill it's usefulness due to coverage of clouds over the study area. To overcome this problem in this study it is decided to utilize microwave data to quantify the water-spread area and in turn the rate of sedimentation of Hirakud reservoir.

1.1 Objectives of the Study

I. To assess the best approach between
   i. per-pixel
   ii. sub-pixel and
   iii. super resolution classifier for the reservoir sedimentation estimation of Hirakud reservoir

II. To evaluate the feasibility of using microwave satellite data for reservoir water-spread area estimation.

CHAPTER 2

LITERATURE REVIEW

2.1 Studies carried out using per-pixel classification approach

Manavalan et al (1990) carried out the storage capacity of the Bhadra and Malaprabha reservoirs in the Krishna river basin using Landsat TM and IRS II digital data respectively. They discuss the possible error limit, due to the omission and commission of mixed pixels involved while estimating the water-spread area. Otherwise the discrepancy between the actual water-spread and the satellite water-spread will lead to a misleading conclusion regarding the rate of sedimentation, especially when there is only marginal deposition of sediments.

Goel et al (2002) discuss that with the use of remote sensing data in conjunction with a geographic information system, the temporal change in water-spread area can be analysed to evaluate the sediment deposition pattern in a reservoir. The reservoir was completed in 1988 and no hydrographie survey has yet been carried out. Under these circumstances, the sedimentation assessment using satellite data guided them for updating the elevation-area-capacity table of the reservoir. The images for nine dates from the IRS-1C satellite, LISS-III sensor have been analysed using the specialized image processing software. The resulting sedimentation rate in the zone of study was about 229 Mm^3/km^2 of catchment area per year.

Jain et al (2002) carried out a remote-sensing based study for the assessment of reduction in capacity in Bhakra Reservoir, located on the Satluj River in the foothills of the Himalayas. They discuss that multi-date remote sensing data (1RS-1B, L1SS II) provided the information on the water-spread area of the reservoir, which was used for computing the change in storage capacity of the reservoir and in turn the sedimentation rate. A comparison of the results shows that the reduction in c apacity assessed using the remote sensing based approach was close to the results obtained from the hydrographic survey.

Jeyakanthan, V.S., (2002) et al carried out capacity estimation of Poondi reservoir located in Tamilnadu, India using satellite data. In this study they utilized IRS-1B & 1C of LISS-II (36 m) and LISS-III (23.5m) sensors data, acquired for seven different elevations ranging from 34.67 m and 41.34 m for the period 1999 & 2000. The water-spread area extracted from the satellite data were used in the trapezoidal formula for the estimation of revised capacity of the reservoir. The comparison of the results with the year 1983 show that the loss in capacity, in the zone under study is 5.09 million cubic metre. If uniform rate of sedimentation is assumed, in 16 years of occurrence of the reservoir then the sedimentation rate in this zone is 0.318 M Cum per year. Comparison of remote sensing results are in agreement with the ground based of hydrographic survey.

Peng et al (2005) used MODerate-resolution Imaging Spectroradiometer (MODIS) data for the flood disaster monitoring of Dongting Lake, China. The storage curve of Dongting Lake for 1995 was obtained using 1:10,000 topographic map data and then a relationship between water level and the lake area was derived. A new relationship between water level and lake area was obtained by processing MODIS images of Dongting Lake from April 2002 to April 2003 and the influence of lake area variation on water level was analysed with the corresponding flood data. It was found that the water level reduction reached 0.64 m for the 1996 flood if the original lake area curve was replaced with the area curve of 2002. This

illustrates that the flood water level has been considerably reduced as a result of the increased area of Dongting Lake since the Chinese Central Government's "return land to lake" policy took effect in 1998.

Renwick et al (2005) examined recent sedimentation rates in 12 reservoirs in two southwest Ohio counties. One of the two counties is primarily urban with high local relief, while the other is primarily agricultural with low relief. In each case a large range of reservoir sizes was studied (< 1 to > 70 km^2 drainage area). In the agricultural county sedimentation rates follow the normal pattern of sedimentation per unit drainage area indicating that the channel systems in the area are likely functioning as sediment sinks. In contrast, in the urban county there is no decrease in sedimentation rate with increasing drainage area, indicating that the channels in that landscape are functioning as efficient conduits and/or net sediment sources. These trends highlight the need to update our reservoir sedimentation databases to determine whether the trends are local or widespread.

Rathore et al (2006) discuss that as per the recommendations of working group for National Action for Reservoir Sedimentation Assessment, Natioanl Institute of Hydrology (NIH) has carried out study on sedimentation studies on 25 reservoirs all over India. One among them is Hirakud reservoir in Mahanadhi basin Odisha studied by the author. Linear Imaging Self Scanning (LISS-III) sensor mounted on the Indian Remote Sensing Satellites (IRS) 1C & 1D data were used to cover the reservoir elevation between 180.69 and 191.89 m. A rule based classification was applied to water index and radiance of NIR band to extract water-spread area. It was found that during 44 (1956-2001) years of operation, the total live storage capacity loss was 984 Mm^3 (which is nearly 17% of the original capacity (5826 Mm^3) of the reservoir) at a rate of 0.376% $year^{-1}$. Thus the satellite data is in immense use for the prediction of rate of sedimentation of reservoirs. Has carried out the capacity survey of Hirakud reservoir, Orrisa, India. They used the IRS-1A satellite data of 5 optimal dates corresponding to various water stages from minimum to maximum drawdown levels in estimating the water spread areas. This was achieved by first thresholding the simple ratio (NIR/RED) image to identify the water pixels and then verifying with the standard FCC. The non-water pixels were then identified with the ratioed (GREEN/NIR) image and removed to have the total water spread. They revised the Elevation – Area curve for Hirakud reservoir based on the analysis of 1988-89 satellite data and it was estimated that the total storage capacity of the reservoir was 6151.30 M.Cu.m., indicating a capacity loss of 1953.70 M.Cu.m. The analysis shows that from 1957 to 1989 there is a continuous decreasing trends in the reservoir capacity.

Bryant Emily S. et.al (1999) studied the Painted Rock Reservoir, southwest of Phoenix, Arizona, which had a storage capacity of about 2.5 million acre-ft in 1959, when dam impoundment was made. When a high flood of record occurred in 1993, it was feared that as much as 500,000 acre-ft of capacity had been lost, and an updated capacity estimate was needed. Because a proposed conventional reservoir survey turned out to be prohibitively expensive, it was decided to investigate the use of Landsat Thematic Mapper remotely sensed data, acquired at multiple reservoir levels, to obtain an updated capacity estimate at a more reasonable cost. Nineteen Landsat Thematic Mapper scenes from 1993 and 1995 were obtained, including reservoir elevations ranging from empty to 5 ft above spillway elevation. Water surface area was determined for each Landsat scene using computer classification of the digital imagery. Investigation results indicate that the Painted Rock Reservoir lost approximately 157,000 acre-ft of storage capacity to sedimentation between 1953 and 1993, significantly less than the 500,000 acre-ft previously feared lost.

Jeyaseelan, A.T. and Thiruvengadachari,S (1997) studied multi-date IRS LISS-II data of 1988-89 to map the water spread of Malaprabha reservoir at five different stages, and compared with those of 1972 being adopted by project authorities. At reservoir levels of 620.15m and 623.54m significant reduction in water spread area was observed while considerable reduction of the order 4 to 9 % was observed at levels 626.53m and 629.98m. The over all reduction in the reservoir capacity between levels of 620.15m and 632.98m was estimated at 3.84 % in a span of 17 years. Similar study was attempted in Gattaprabha reservoir using mulitidata IRS, LISS-II data. The overall reduction in capacity of the reservoir between levels 635.24m and 662.94m was computed to be 8.6% in a 16 year period between 1974 and 1900.

Raju et al carried out the field radiometric and satellite data analysis for Upper Lake, Bhopal. Satellite data used were of TM sensor for the month of February. Synchronous collection of field data was completed starting two days prior to satellite over pass date. The field data were collected before noon in all days. Field radiometric data showed high correlation with Total Suspended Sediment (TSS). TSS was in the range from 38 to 70 ppm. Only one reading was of 110 ppm. Thus the range of TSS was small for this study. A regression equation was fitted between radiometric Bands 1 and 2 and TSS. TSS was independent variable in the equation. The correlation coefficient and error of estimate were respectively 0.8843 and 5.8 ppm. Satellite data were also classified into five classes using supervised method for TSS concentrations.

Peng Dingzhi et al (2006) estimated storage curve of Fengman reservoir in China based both on traditional and remote sensing approach. They discuss that there are many different classification methods or models for extraction of water-spread area of a reservoir such as the density-slicing approach and the normalized difference water index (NDWI) method. The comparison showed that the reservoir storage curve estimation based on RS data is reasonable and economical.

Reservoir sedimentation study using per-pixel approach has been reported by Mohanty (1986) for the Hirakud Reservoir in India, Vibulsresth (1988) for the Ubolratana Reservoir in Thailand, Manavalan (1993) for the Malaprabha Reservoir in India, Jeyaseelan and Thiruvengadachari (1997) for the Kuttiyadi Hydel Reservoir in India, Chandrasekar and Jeyaseelan (2000) for the Tawa Reservoir in India, Jeyakanthan (2002) for the Poondi Reservoir in India, Goel (2002) for the Bargi Reservoir in India, Jain (2002) for the Bhakra Reservoir in India, Magome (2002) for the Yagisawa Reservoir in China and Peng (2006) for the Fegman Reservoir in China, Pankaj Mani (2007) for the Maithon Reservoir in India.

2.2 Studies carried out using Sub-pixel classification approach

Quarmby et al. (1992) discuss the use of spectral unmixing *viz.*, linear mixture modelling for crop area estimation. Multi-temporal AVHRR dataset of 9 dates of Northern Greece were used and the input to the model was obtained using supervised classification of SPOT HRV images. The proportions of maize, rice, cotton and wheat were correlated with official statistics from 18 village units for comparison of area of each category and the accuracy was 89% showing the performance of the mixture model. The results showed that the linear mixture modelling (LMM) has potential for operational crop area monitoring on a regional scale.

Foody et al (1994) estimated the sub-pixel land cover composition using a LMM and Fuzzy membership function. For both approach, a significant correlation co-efficients, all >0., between the actual and predicted proportions of a land cover type within a pixel were obtained.

The mapping of land cover components, vegetation, in particular, with the help of NOAA-AVHRR (Advanced Very High Resolution Radiometer) data was discussed by Shimabukuro et al (1997). Fraction images of vegetation, soil and water/shade were derived from a set of six AVHRR images in the Sao Paulo state, Brazil using linear mixing model. Constrained least squares approach was employed and a global vegetation cover map was available for comparison. In addition, NDVI values were computed and there was a good correlation between the NDVI values and the vegetation fraction obtained through unmixing. This paper gives an insight into the use of linear mixing model for mapping vegetation cover. Though the aim of the paper was to extract vegetation details, it brings out the importance of soil and shade fraction images, which aid in a better understanding of the spectral response of the other land cover types.

Shimabukuro and Novo (1997) proposed a methodology viz., mixing model formapping of flood habitats in the Amazon basin. Two adjacent scenes of Landsat TM available in digital format were used for the study. The transformation of digital numbers to spectral reflectance values and radiometric rectification of images was carried out. Assessment of the rectification process and the consequent application of mixing model yielded a classified map of the flood habitats. Three end members were chosen as input for the mixing model and the map thus obtained was compared with a reference map derived from visual interpretation. Flood habitats mapping using mixing model yielded a good classification result. Though accuracy assessment was not carried out, the paper proposes a new methodology namely, mixing model for the purpose of mapping flood habitats to overcome the limitations of per-pixel classification.

Casals-carrasco (2000) applied spectral mixture mixture analysis (SMA) for terrain evaluation using Landsat-TM and Panchromatic images. The author compared the results obtained by traditional supervised rules such as Maximum Likelihood Classifier (MLC) with spectral mixture analysis. The results showed SMA was efficient in deriving more information image data compared to the conventional techniques.

The use of spectral unmixing as a tool for bauxite and laterite mineral targeting and mapping in the Koraput district, Odisha, India was carried out by Das (2002). End members were chosen using the PPI technique. The characteristic laterite cappings in the hills containing bauxite was observed in the Landsat TM image and such region is generally devoid of vegetation cover. MTMF, which performs partial unmixing based on the end members supplied by the users, was used to unmix the abundances of laterite/bauxite, vegetation and red soil. This study has helped in the discrimination of similar regions in the nearby hills of the Koraput town.

Lu Dengsheng et al (2003) says that many research projects require accurate delineation of different secondary succession (SS) stages over large regions/subregions of the Amazon basin. However, the complexity of vegetation stand structure, abundant vegetation species, and the smooth transition between different SS stages make vegetation classification difficult when using traditional approaches such as the maximum likelihood classifier (MLC). Most of the time, the MLC distinguishes only between forest and non-forest. It has been difficult to

accurately distinguish stages of SS. Therefore the authors applied a linear mixture model (LMM) approach to classify successional and mature forests using Thematic Mapper (TM) imagery in the Rondoˆnia region of the Brazilian Amazon. Three endmembers (i.e., shade, soil, and green vegetation or GV) were identified based on the image and a constrained least-squares solution was used to unmix the image. This study indicates that the LMM approach is a promising method for distinguishing successional and mature forests in the Amazon basin using TM data. It improved vegetation classification accuracy over that of the MLC. Initial, intermediate, and advanced successional and mature forests were classified with overall accuracy of 78.2% using a threshold method on the ratio of shade to GV fractions, a 7.4% increase over the MLC. The study implies the LMM approach distinguishes different species in a forest and therefore more promising results can be obtained than the MLC.

Paintera et al (2003) used an automated model that retrieves sub-pixel snow-covered area and effective grain size from Airborne Visible/Infrared Imaging Spectrometer (AVIRIS) data. The model analyzes multiple end-member spectral mixtures with a spectral library of snow, vegetation, rock, and soil. They derived the snow spectral end-members of varying grain size from a radiative transfer model. End-member spectra for vegetation, rock, and soil were collected in the field and laboratory. The sub-pixel estimates of snow-covered areas were validated with the fine-resolution aerial photographs. The RMS error for the combined set of fraction images was 4%. This study shows that the authors have used the high resolution data to validate the results of sub-pixel output and such validation proves that un-mixing produces less error.

Lobell and Asner (2004) says that the knowledge of the distribution of crop types is important for land management and trade decisions, and is needed to constrain remotely sensed estimates of variables, such as crop stress and productivity. The Moderate Resolution Imaging Spectro-radiometer (MODIS) data was used by the authors for large scale crop type mapping. Further the authors say that because of sub-pixel heterogeneity, the application of traditional hard classification approaches to MODIS data may result in, significant errors in crop area estimation. Therefore, they developed and tested a linear un-mixing approach with MODIS that estimates sub-pixel fractions of crop area based on the temporal signature of reflectance throughout the growing season. In this method, the authors used probabilistic temporal un-mixing (PTU), technique for the identification of end-member sets. The results of this study demonstrates the importance of sub-pixel heterogeneity in cropland systems, and the potential of temporal un-mixing to provide accurate and rapid assessments of land cover distributions using coarse resolution sensors, such as MODIS.

Richard Fernandes et al (2004) carried out a comparative study using five algorithms for mapping sub-pixel land cover fractions and continuous fields of vegetation properties in their study area (Boreas Ecosystem Atmosphere Experiment (BOREAS) region in Canada). The algorithms include a conventional ‘‘hard’’, per-pixel classifier, a neural network, a clustering/look-up-table approach, multivariate regression, and linear least squares inversion. The comparison reveals that the ‘‘Hard’’ classification performed poorly in estimating proportions or continuous fields. The neural network, look-up-table and multivariate regression algorithms produced good results. However, all three methods exhibited substantial biases with the distant treatment due to the characteristics of the training data. Linear least squares inversion offers a relatively unbiased estimation of sub-pixel proportion and fraction mapping as it avoids calibration to the a priori distribution of land cover in the training data.

Simic et al (2004) carried out a study to address the issues related to spatial scaling of net primary productivity (NPP). The main objective of the study is to develop algorithms for spatial scaling of NPP using sub-pixel information. NPP calculations were performed using the Boreal Ecosystem Productivity Simulator (BEPS). The area of interest is near Fraserdale, Ontario, Canada. It was found from the investigation that lumped (coarse resolution) calculations can be considerably biased (by +14.9% on average) from the distributed (fine resolution) case. Based on these results, algorithms for removing these biases in lumped NPP are developed using sub-pixel land cover type information. The correlation between the distributed NPP and lumped NPP is improved from r^2=0.16 to r^2=0.59 after the correction. In addition, sub-pixel leaf area index (LAI) information is used to reduce the remaining biases. After the LAI correction, the correlation is further improved to r^2=0.90.

Rodrigo Sagardia (2005) used sub-pixel classifier for wetland mapping in the Cuitzeo Lake, Mexico and mapped the different communities of plants using MODIS images and linear mixture modeling. It was shown that the fractions present at sub-pixel level could be estimated with a good degree of accuracy, lying within 25% of the actual values. The performance of the soft classifier is at least three times higher than a hard classification of an artificial image of the same pixel size in areas that show mixed pixels.

Peddle and Smith (2005) used spectral mixture analysis (SMA) to quantify the area abundance of plants, soils and shadows at sub-pixel scales with the aim of improving extraction of plant biophysical and structural information from remote sensing data. Different measurement strategies were tested in the field for acquiring reference end-member spectra of crop vegetation, soil and shadows using a field spectro-radiometer for a set of potato plots in western Canada. End-member fractions derived from excised leaves, cultivated soil and shadowed vegetation spectra showed the best agreement with ground truth data, with differences of only ±3.3%. These sub-pixel scale fractions were used in regression analyses to predict leaf area index, biomass and plant width with an average r^2 value of 0.85 from SMA shadow fraction, which was a substantial improvement over the best VI results from NDVI, NGVI and SR (average r^2 = 0.53). Perspectives on SMA at different stages in the growing season and for different crop types are provided with a recommendation that further SMA research is warranted for local to regional scale agricultural crop monitoring programmes.

Mertens et al (2006) say that soft classification techniques avoid the loss of information characteristic to hard classification techniques when handling mixed pixels. Sub-pixel mapping is a method incorporating benefits of both hard and soft classification techniques. They developed an algorithm based on sub-pixel/pixel attractions. The design of the algorithm is accomplished using artificial imagery but testing is done on artificial as well as real synthetic imagery. The algorithm was evaluated both visually and quantitatively using established classification accuracy indices. The resulting images show increased accuracy when compared to hardened soft classifications.

de Asis and Omasa (2007) used models such as Universal Soil Loss Equation(USLE) and its subsequent Revised Universal Soil Loss Equation (RUSLE) to generate the quantitative estimates necessary for designing soil conservation measures. However, large-scale soil erosion model-factor parameterization and quantification is difficult due to the costs, labor and time involved. Among the soil erosion parameters, the vegetative cover or *C* factor has been one of the most difficult to estimate over broad geographic areas. The *C* factor represents the effects of vegetation canopy and ground covers in reducing soil loss.

Traditional methods for the extraction of vegetation information from remote sensing data such as classification techniques and vegetation indices were found to be inaccurate. Thus, this study presents a new approach based on Spectral Mixture Analysis (SMA) of Landsat ETM data to map the *C* factor for use in the modeling of soil erosion. A desirable feature of SMA is that it estimates the fractional abundance of ground cover and bare soils simultaneously, which is appropriate for soil erosion analysis. They used a linear SMA (LSMA) model and performed a minimum noise fraction (MNF) transformation and pixel purity index (PPI) on Landsat ETM image to derive the proportion of ground cover (vegetation and non-photosynthetic materials) and bare soil within a pixel. The end-members were selected based on the purest pixels found using PPI with reference to very high-resolution QuickBird image and actual field data. Results showed that the *C* factor value estimated using LSMA correlated strongly with the values measured in the field. The correlation coefficient (*r*) obtained was 0.94. A comparative analysis between NDVI- and LSMA-derived *C* factors also proved that the latter produced a more detailed spatial variability, as well as generated more accurate erosion estimates when used as input to RUSLE model.

Weng Qihao and Lu (2008) carried out a study based upon a spectral un-mixing model for characterizing and quantifying urban landscape changes in Indianapolis, Indiana, the United States, and for examining the environmental impact of such changes on land surface temperatures (LST). Three dates of Landsat TM/ETM+ images, acquired in 1991, 1995, and 2000, respectively, were utilized to document the historical morphological changes in impervious surface and vegetation coverage and to analyze the relationship between these changes and those occurred in LST. Three fraction end-members, i.e., impervious surface, green vegetation, and shade, were derived with an unconstrained least-squares solution. Correlation analyses were conducted to investigate the changing relationships of LST with impervious surface and vegetation coverage. Results indicate that multi-temporal fraction images were effective for quantifying the dynamics of urban morphology and for deriving a reliable measurement of environmental variables such as vegetation abundance and impervious surface coverage.

Carola et al (2010) used Landsat overpasses from six different dates and developed a robust linear model to predict sub-pixel fractions of water cover in the Doñana Biological Reserve, Spain. The model was applied to a time series of 174 Landsat TM and ETM+ images to reconstruct the flooding regime of a system of small temporary ponds and to study their spatio-temporal changes in a 23-year period. The authors tried to differentiate natural fluctuations from trends in hydrologic variables (*i.e.*, hydroperiod shortening) that may threaten the preservation of the system. Although medium-resolution remote sensing data have rarely been applied to monitor the small-sized wetlands, this study evidences its utility to understand the hydrology of temporary ponds at a local scale using fraction images.

Ruescas et al (2010) estimated the percentage of burnt land at sub-pixel scale using the Advanced Very High Resolution Radiometer (AVHRR) through a simple approach. This methodology is based on multi-temporal spectral mixture analysis (MSMA), which uses a normalized difference vegetation index (NDVI) and a land-surface temperature (LST) image as input bands. The area of study is located in the Alcalaten region in Castellon (Spain), a typical semi-arid Mediterranean region. The results have shown an extension of approximately 55 km^2 affected by fire, which is only 5% lower than the statistic reports provided by the Environmental Ministry of Spain. Further, the authors have included a map of the area showing the percentage of estimated burnt area per pixel and its associated

uncertainties. The map was validated through supervised classification of an Airborne Hyperspectral Sensor (AHS) image. Results have shown a high accuracy, with a mean error of 6.5%.

Silván-Cárdenas and Wang (2010) carried out a study using sub-pixel classification techniques based on linear and nonlinear spectral mixture models in order to identify the best possible classification technique for repeatable mapping of saltcedar (*Tamarix* spp.) canopy cover along the Forgotten River reach of the Rio Grande. The accuracy of sub-pixel canopy cover was assessed through a 1-m spatial-resolution hyper-spectral image and field measurements. Results indicated that the accuracy of the fully constrained linear spectral un-mixing method increased (from 67% to 77%) when the classes were represented with several image spectra.

2.3. Studies carried out using Super resolution mapping approach

Tatem, A. J. et al (2002) examined that landscape pattern represents a key variable in management and understanding of the environment, as well as driving many environmental models. Remote sensing can be used to provide information on the spatial pattern of land cover features, but analysis and classification of such imagery suffers from the problem of class mixing within pixels. Fuzzy classification techniques can estimate the class composition of image pixels. However, their output provides no indication of how such classes are distributed spatially within the instantaneous field of view represented by the pixel. Techniques to provide an improved spatial representation of land cover targets larger than the size of a pixel have been developed, however, the mapping of sub-pixel scale land cover features has yet to be investigated. We recently described the application of a Hopfield neural network technique to super-resolution mapping of land cover features larger than a pixel, using information of pixel composition determined from fuzzy classification, and (was but) now show how our approach can be extended in a new way (added) to predict the spatial pattern of sub-pixel scale features. The network converges to a minimum of an energy function defined as a goal and several constraints. Prior information on the typical spatial arrangement of the particular land cover types is incorporated into the energy function as a constraint. This produces a prediction of the spatial pattern of the land cover in question, at the sub-pixel scale. The technique is applied to synthetic and simulated Landsat TM imagery, and compared to results of an existing super-resolution target identification technique. Results show that the new approach (was Hopfield neural network) represents a simple, robust and efficient tool for super-resolution land cover pattern prediction from remotely sensed imagery.

Foody et al., (2005) discusses methods for mapping the waterline at a subpixel scale from a soft image classification of remotely sensed data are evaluated. Unlike approaches based on hard classification, these methods allow the waterline to run through rather than between image pixels and so have the potential to derive accurate and realistic representations of the waterline from imagery with relatively large pixels. The most accurate predictions of waterline location were made from a geostatistical approach applied to the output of a soft classification (RMSE52.25 m) which satisfied the standards for mapping at 1 : 5000 scale from imagery with a 20 m spatial resolution.

Nguyen, M. Q et al (2006) explains that superresolution mapping is a set of techniques to increase the spatial resolution of a land cover map obtained by soft-classification methods. In addition to the information from the land cover proportion images, supplementary information at the subpixel level can be used to produce more detailed and accurate land

cover maps. The proposed method in this research aims to use fused imagery as an additional source of information for superresolution mapping using the Hopfield neural network (HNN). Forward and inverse models were incorporated in the HNN to support a new reflectance constraint added to the energy function. The value of the function was calculated based on a linear mixture model. In addition, a new model was used to calculate the local endmember spectra for the reflectance constraint. A set of simulated images was used to test the new technique. The results suggest that fine spatial resolution fused imagery can be used as supplementary data for superresolution mapping from a coarser spatial resolution land cover proportion imagery.

Heltin, G. C. and Vani, K. (2010) discusses that super resolution mapping is a set of techniques to increase the spatial resolution of a land cover map obtained by soft classification methods. Linear spectral unmixing have been developed to estimate the class composition of image pixels, but their output provides no indication of how these classes are distributed spatially within the instantaneous field of view represented by the pixel. The use of a Hopfield neural network to map the spatial distribution of classes more reliably using prior information of pixel composition determined from linear spectral unmixing was investigated. The output from the linear spectral unmixing which is a set of area proportion images for each land cover class is given as input to the HNN. The network converges to a minimum of the energy function which is defined by the goals and constraints of the super resolution mapping task. The minimum of the energy of the network represents the best guess map of the given satellite image. The technique was applied to both real and simulated Landsat images, and the resultant maps provided an accurate and improved representation of the area under study. The Hopfield neural network represents a simple, robust, and efficient technique, and results suggest that it is a useful tool for identifying land cover targets from remotely sensed imagery at the subpixel scale.

Muad, A. M., and Foody, G. M. (2012) carried out the potential of super-resolution mapping (SRM) techniques for the representation of lakes was evaluated using both an established and a newly proposed method. Both super-resolution mapping techniques were typically able to provide representations that were visually and quantitatively more realistic than standard hard classifications. The new technique was able to represent more small lakes than the established technique. The results also demonstrate the value of using a time series of images as input to the super-resolution analysis, enabling researchers to usefully exploit the typically fine temporal resolution of coarse spatial resolution sensors for land cover mapping.

Holland, J., & Aplin, P. (2013) explains that the bracken (Pteridium aquilinum) fern is environmentally significant due to its great abundance and swift colonisation, and its perception as a problem plant in degrading agricultural or ecologically sensitive land. Various attempts have been made to map bracken using remote sensing, but these have proved relatively unsuccessful, often apparently constrained by the lack of spatial detail associated with medium spatial resolution satellite sensors such as the Landsat series. In this study, bracken was characterised using a combination of 30 m Landsat sensor imagery and 4 m IKONOS imagery. Different classification techniques were compared, including hard maximum likelihood classification and a super-resolution approach comprising soft classification and sub-pixel contouring. These techniques were applied to a range of image dates, including summer, winter and multitemporal images. Image analysis was supported by extensive field data collection, comprising both a land cover survey and stakeholder interviews. For the hard classified Landsat sensor imagery, the summer image proved least

able to characterise bracken, due largely to the spectral similarity between (green) growing bracken and grasses and other vegetation. Following soft classification of the multitemporal Landsat image, super-resolution sub-pixel contouring was applied to identify the boundary of bracken patches. Predicted bracken boundaries were assessed against actual boundaries identified using field observation and IKONOS image interpretation. For comparison, the bracken boundaries identified through hard classification (i.e. using pixel edges) were also assessed against the actual boundaries. Overall, the spatial accuracy of the super-resolution approach proved considerably higher than that of hard classification.

Bouthayna Msellmi, et al., (2016) explains that hyperspectral image has a great ability to discriminate the ground object by providing a fine spectral resolution image. This progress in hyperspectral technologies causes some problems including mixed pixel problem, which is a main issue for hyperspectral image classification and target detection because more than one class can be detected in a single pixel. In order to identify mixed pixel composition for different classes, many spectral unmixing methods have been proposed. Even thought spectral un-mixing methods may estimate the proportions of classes in a mixed pixel, they failed to describe the spatial distribution of each land cover class within a mixed pixel. In 1997 the technical mapping sub-pixel was been proposed by Atkinson to solve the over mentioned problem, by transforming fractions images into a high spatial resolution map. Most proposed sub-pixel mapping methods are based on spatial interpixel dependence; also the scale factor is selected arbitrarily and beforehand. In our paper we propose an adaptive sub-pixel mapping algorithm. In order to improve sub-pixel mapping accuracy, we consider spatial correlation between sub-pixels and we suggest an adaptive choice of scale factor. The experimental results with synthetic image from USGS spectral library show that the proposed algorithm successfully constructs the different spatial distributions of classes in a mixed pixel.

2.4. Studies carried out using Microwave Satellite Data

Bazi et al (2007) stated that thresholding is a key point in the histogram-based approach and pattern recognition The estimation of the statistical parameters of “object” and “background” classes by the expectation–maximization algorithm, under the consideration of these two classes follow a generalized Gaussian (GG) distribution. The adoption of such a statistical model as an alternative to the more common Gaussian model is motivated by its attractive capability to approximate a broad variety of statistical behaviors with a small number of parameters.

Marzano et al., (2011) performed SAR-based estimates of surface water extent which are confounded by difficulties with wind roughening of the water surface for the wavelengths used by most existing sensors and also by high rain- fall intensities The experiment conducted in the year 2011, work was devoted to explore the potential of X-band high-resolution detection and retrieval of rainfall fields from space using X-SAR signal backscattering amplitude and interferometric phase, evaluated the effects of spatial resolution degradation by precipitation and inhomogeneous beam filling when comparing to other satellite-based sensors.

Gstaiger et al., (2012) conducted a simple threshold-based approach with additional morphological operators which can quickly deliver water masks of very high accuracies. Since the thresholds are defined empirically until now using histogram information, it is not always possible to directly choose the thresholds leading to the highest possible accuracy of

the water mask. A further study of the findings by comparing multiple thresholds revealed that within a certain interval a deviance from the best threshold resulted in water masks with very high accuracies. Another important aspect of analyzing the data from remote sensing was product validation. It was necessary but very difficult to get accurate high-quality ground-based truth information and also suit the time of over passing the satellite. In the event of a lack of ground-based reality, reference data can also be manually derived but must be considered highly dependent on the subjective evaluation The choice of the sensor which will be used to detect water areas depends on the product being implemented. TerraSAR-X data provided very high detail and precision water masks but only cover small areas depending on the acquisition mode. Envisat-1 ASAR's water masks cover a wider area and are even less affected by threshold variations, but provide less detail because of the lower spatial resolution.

O'Grady et al., (2013) examined the relationship of C-band radar backscatter from the Advanced Synthetic Aperture Radar on board the Envisat satellite with the local angle of incidence, which influenced the received signal, particularly in the modes of sensor operation that use the full swath of the orbit track. Linear regression is carried out for each pixel throughout a large time series of SAR data. Class separability analysis shown that the potential to use the resultant coefficients as an absolute threshold values for distinguish between classes of vegetation and geology, where cloud cover may preclude the use of optical data**.** It is observed that the separability between water and land is greatly higher using the slope coefficient than using backscatter value, which may be of great benefit in the remote sensing of water where cloud cover is present from which SAR is highly independent. This was especially the case when considering the observed overlapping of backscatter values from water, with values from Aeolian sand and lacustrine and alluvial sediments, rendering the use of backscatter alone problematic.

Amitrano et al.,(2014)explored the performances and the opportunities in the year 2014 provided by the European satellite Sentinel-1 for water resource management applications in low-income countries. The analysis was supported by a synthetic aperture radar (SAR) simulator, which allowed the quantification of the expected characteristics of Sentinel-1 products in three applications: interferometric digital elevation models (DEMs) generation, land cover mapping and estimation of water volumes retained by small reservoirs. The obtained results quantitatively shown that Sentinel-1 data characteristics were fully suitable for most of the small reservoir monitoring application.

Schumann & Moller (2015) conducted detailed analysis on applications of microwave remote flood inundation sensing, focusing primarily on synthetic aperture radar (SAR) in a variety of natural and man-made environments and its strengths and limitations are listed such as: "Image file size is considerably larger than commonly processed SAR images with pixel spacing typically larger than commonly processed images i.e.,10 m or 30 m, making computer processing for global classification methods, i.e. algorithms applied to the entire image swath rather than just a small subset, challenging"and the work concluded with a brief account on perspectives and emerging technologies.

Duy (2015) suggested a technique called Valley-Emphasis method of automatic water extraction, employed to identify surface water bodies at three areas, having different landscapes and covers, using Sentinel-1A IW images widely used automated Otsu method was performed for extracting surface water bodies to compare proposed method. The results of proposed method were compared to those of Otsu method and the reference data such as

Landsat 7, 8 gave the highest Completeness (User accuracy), Correctness (Producer accuracy) and Quality (Overall accuracies) at 98.8%, 90.7 % and 89.7 %, respectively. The employed method was straightforward, easy to implement and may be applied for other areas even at regional or global scales. This method also improves automatic identification level of surface water bodies, providing essential information for flood disaster research.

Potin et al.(2016) gave an overview of the overall mission status and Sentinel-1A routine operations activities that started in June 2015 following the operational qualification phase, in terms of mission achievements, mission observation scenario, ground segment operations, throughput and data access. It also provided few examples of applications based on Sentinel-1 data.

Liu (2016) stated various limitations and recommendations which are documented for the experiment conducted "Analysis of Sentinel-1 SAR data for mapping standing water in the Twente region" such as "The standing water area in observation is as much as 10 m × 5 m randomly distributed in the fields. However, the resolution of Sentinel-1 images is 10 m. One problem would be that the standing water area is relatively small compared to the pixel size of the SAR observations" and "backscatter derived from a region will cause the signal of standing water mixed with other surface signals, which will add uncertainty to the result".“Based on the field-scale backscatter changes, standing water is difficult to delineate from the Sentnel-1 images due to the uncertainties. Those uncertainties include different surface conditions in each agricultural field, soil moisture, vegetation characteristics and agricultural activities. Those factors vary from temporal and spatial scale, like farming practices and atmospheric forcing”.

Nagler et al., (2016) studied of the impact of polarization, and generated the maps of melting snow using data of the VV-polarized channel, the VH-polarized channel and a combined VV- and VH-based channel using a weighting function that accounted for effects of the local incidence angle. Comparisons were performed with snow maps derived from Landsat images over study areas in the Alps and in Iceland. The pixel-by-pixel comparisons showed good agreement between the snow products of the two sensors, with the best performance for retrievals based on the combined (VV and VH) channel and a minor decline for the VH-based product. The VV-based snowmelt extent product shows a drop-off in quality over areas with steep terrain because of the decreasing backscatter contrast of snow-covered versus snow-free surfaces on fore-slopes. The investigations demonstrated the excellent capability of the Sentinel-1 mission for operational monitoring of snowmelt areas.

Twele et al., (2016) performed Sentinel-1-based flood mapping by a fully automated processing chain with an automated Sentinel-1-based processing chain designed for flood detection and monitoring in near-real-time (NRT) was proposed. Since no user intervention is required at any stage of the flood mapping procedure, the processing chain allows deriving time-critical disaster information in less than 45 min after a new data set is available on the Sentinel Data Hub of the European Space Agency (ESA). aweb-based service that regularly informs users about the current flood conditions in a given area of interest. The thematic accuracy of the thematic processor has been assessed for two test sites of a flood situation at the border between Greece and Turkey with encouraging overall accuracies between 94.0% and 96.1% and Cohen’s kappa coefficients (κ) ranging from 0.879 to 0.910. The accuracy assessment, which was performed separately for the standard polarizations (VV/VH) of the interferometric wide swath (IW) mode of Sentinel-1, further indicates that under calm wind

conditions, slightly higher thematic accuracies can be achieved by using VV instead of VH polarization data.

Chauhan & Srivastava (2016) tested the capabilities of the dual polarimetric Envisat-1 ASAR and Landsat ETM+ data that had been investigated for the land cover mapping. A comprehensive evaluation of the sensitivity of the cross-polarized (VH)/like-polarized (VV) Envisat-1 ASAR and optical data for various land cover classes had been done and a class separability analysis was performed under different band combinations. In order to ensure maximum information retrieval, the bands Microwave Polarization Difference Index MPDI and Normalized Difference Vegetation Index NDVI have also been incorporated. The separability among the class pairs have been analyzed using the Transformed Divergence procedure while the classification has been carried out using the Maximum Likelihood supervised classifier. The results of sensitivity analysis indicated that the vegetation is highly sensitive to the VH band owing to volume scattering while the built-up class could be more accurately distinguished in the VV band due to the corner reflector effect. The separability analysis further revealed that with the fusion of optical-VH polarized SAR data and the introduction of MPDI band to the multi-polarized SAR data, the separability among various class pairs were greatly improved. The Landsat ETM+ and VH backscatter data fused image concluded the highest classification accuracy of 91.25% with the kappa coefficient of 0.90 and demonstrated the potential in land cover assessment and monitoring.

Bolanos et al., (2016) analyzed the technical requirements of the Radarsat-2 beam mode, polarization and resolution by a threshold-based procedure to map locations of non-vegetated water bodies after the ice break-up is performed and complemented with a texture-based indicator to capture the most homogeneous water areas and automatically delineated their extents. Some strategies to cope with the radiometric artifacts of noise inherent to Synthetic Aperture Radar (SAR) images are also discussed. Results shown that Radarsat-2fine mode captured 88% of the total water area in a fully automated way. This will greatly improve current operational procedures for surface water monitoring information and impact a number of applications including weather forecasting, hydrological modeling, and drought/flood predictions.

Pham-Due et al., (2017) observed Sentinel-1 SAR observations over the Mekong Delta in 2015 were processed and the derived surface water maps were compared to corresponding MODIS/Terra-derived surface water maps at 500 m spatial resolution. Temporal correlation between these two products is very high (99%) with very close water surface extents during the dry season when cloud contamination is low and this study highlights the applicability of the Sentinel-1 SAR data for surface water monitoring, especially in a tropical region where cloud cover can be very high during the rainy seasons.

Garkusha et al., (2017) developed an empirical model to build maps of moisture of the research study site for different times shown water surface incorrectly and excessively moistened parts of land are clearly highlighted, where the precipitation quantity was considerable according to the weather station, the relative humidity of 100% was observed.

Parasad et al., (2018) realized that the SAR data was capable in assessing the sedimentation in a reservoir. SAR data can be used to extract water spread, which is a prime requisite of remote sensing approach to assess sedimentation. Moreover, the high repeat period of Sentinel-1 makes its ideal sensor for mapping water spread at very close interval, which further improves sedimentation assessment which reduces the error in considering the volume

between two dates as trapezoid. It was noted that the remote sensing approach can be used as substitute to hydrographic surveys; however, the capacity or sedimentation assessment will always be more accurate through hydrographic surveys. Keeping in mind the cost and time required for the hydrographic surveys, it was recommend that these surveys can be done at large duration, whereas, sedimentation assessment through remote sensing approach can be carried out at shorter time interval.

Federico Filipponi Istituto (2019) provided a standard generic workflow to preprocess Copernicus Sentinel-1 GRD data which aimed to apply a series of standard corrections, and to apply a precise orbit of acquisition, remove thermal and image border noise, perform radiometric calibration, and apply range Doppler and terrain correction. Additionally, this workflow allows spatially snapping of Sentinel-1 GRD products to Sentinel-2 MSI data grids, in order to promote the use of satellite virtual constellations by means of data fusion techniques. The presented workflow allows the production of a set of preprocessed Sentinel-1 GRD data, offering a benchmark for the development of new products and operational down-streaming services based on consistent Copernicus Sentinel-1 GRD datasets, with the aim of providing reliable information of interest to a wide range of communities.

Chen et al., (2020) investigated the potential use of Sentinel-1 data for monitoring wetland water level changes in China's Momoge National Nature Reserve. Interferometric Synthetic Aperture Radar (InSAR) technique was used for monitoring wetland water levels. However, its capability in monitoring wetland water level changes with Sentine-1 data was not thoroughly investigated. The results of water level changes from InSAR processing show no agreement with in-situ measurements during most growth stages. Based on the findings, we can conclude that although the interferometric coherence of the Sentinel-1 C-VV data is high enough, the data is generally unsuitable for monitoring water level changes in marsh wetlands of China's Momoge National Nature Reserve.

CHAPTER-3

STUDY AREA AND DATA USED

3.1 Location

The Hirakud dam is located at the latitude and longitude of 21.57^{o} N and 83.87^{o} E. The project is constructed across Mahanadi and is located 15 km from Sambalpur in Odisha. It is a multipurpose project with objective of irrigation, power generation and flood control. Powerhouses are located at Burla and Chiplima. The reservoir is located in Jharsuguda, Bargarh and Sambalpur districts of Odisha. Mahanadi deltas in Puri and Cuttack districts of Odisha are protected from floods by this project. The study area is shown in Fig.3.1.

3.2 Catchment Characteristics

Hirakud Dam was built across the Mahanadi River, about 15 km from Sambalpur in the state of Odisha in India. The project was completed during 1957 and contains the world's largest earthen dam. Hirakud Dam is one of the longest dams in the world, about 26 km in length. It was the first major multipurpose river valley project started after India's independence. The Hirakud reservoir has a catchment area of 83,400 km² (Figure 3.2) and the live storage capacity is 5,842 MCM, whereas the gross storage capacity is 8105 MCM.

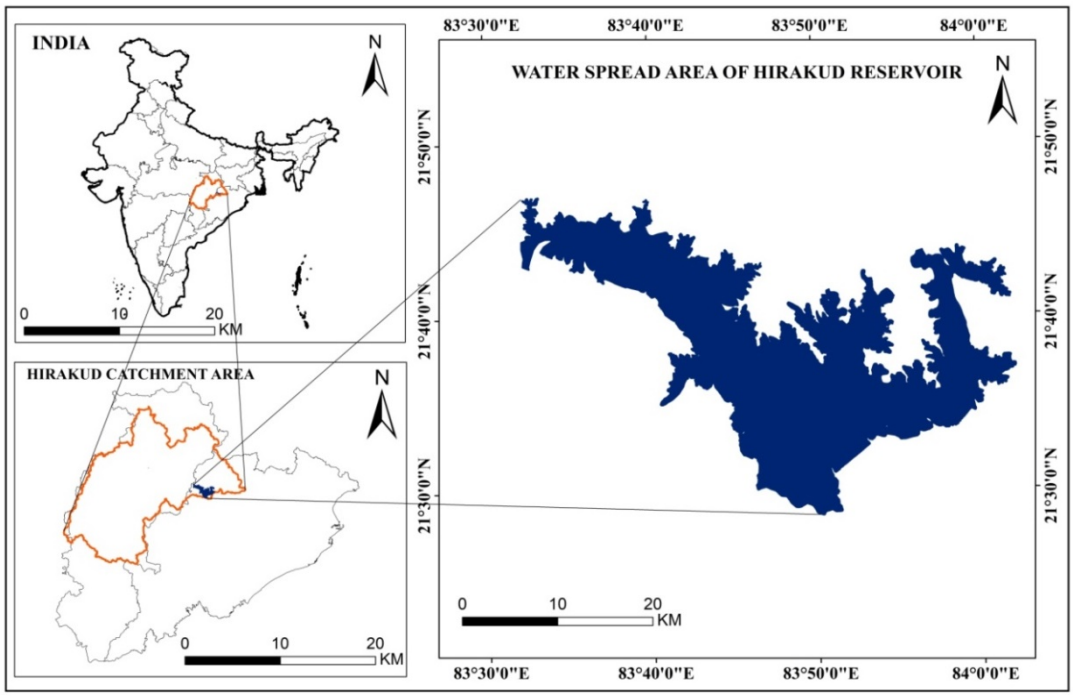

Figure **Error! No text of specified style in document.**.1 Location map of Hirakud

3.4 Hirakud Dam

On 15th March 1946, Sir Howthrone Lewis laid the foundation for the construction of the longest man-made dam in the world which extends 26 Km in length. It was constructed in between 1948 and 1957 with estimated cost of 1.01 billion. The quantity of earthwork in the

dam was estimated to be 18,100,000 m^3 and concrete quantity of 1,070,000 m^3 and the area lost in the construction of the dam was about 596.36 Km^2. Top dam level of 195.680 m, full reservoir level 192.024 m and dead storage level 179.83 meter, the reservoir formed an artificial lake of 743 Km^2 (Figure 3.2). The main purpose of the dam was to protect the flood in Mahanadi deltas and it protects about 9500 Km^2 of delta area, the secondary purpose being the irrigation it irrigates 1,08,385 Hectares of Rabi crops and 1,59,106 Hectares of Kharif crops. Hirakud reservoir's salient features are given in Table 3.1.

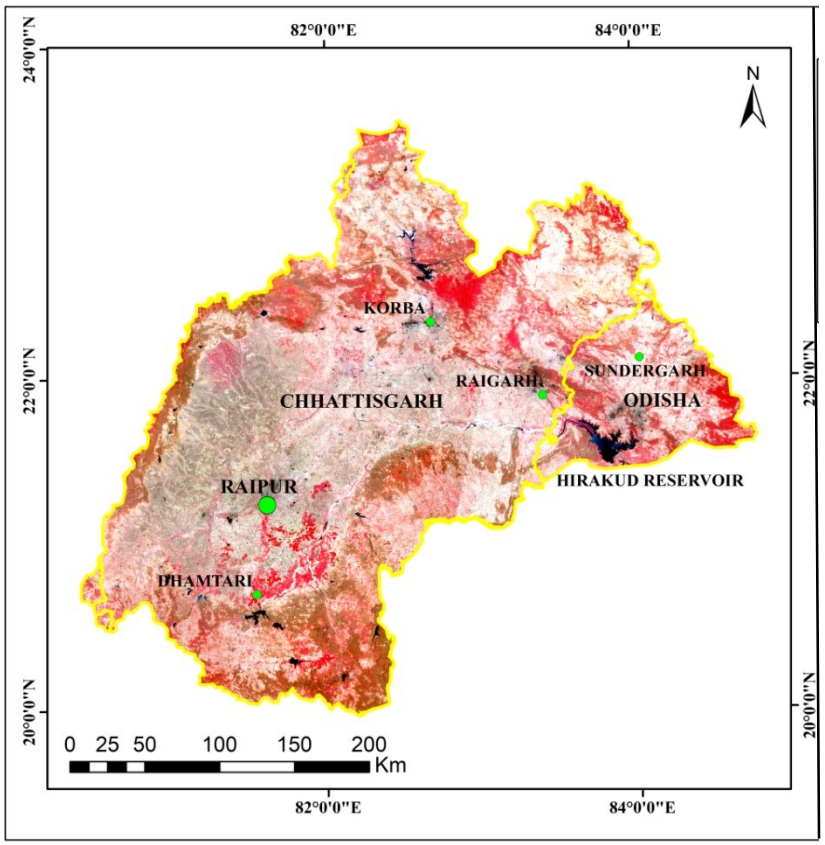

Figure 3.2 Catchment area of Hirakud reservoir

3.3 Climate

The catchment area is by tropical climate, characterized by high temperature, high humidity, medium to high rainfall and short and mild winters. The south west monsoon normally sets in between 5th June and 10th June in the coastal plain, by 1st July the whole of the state is under the full sway of the south-west monsoon. By 15th October, the south-west monsoon withdraws completely from the state.

The temperature in this region varies from 14 °C to 40 °C. The average highest monthly temperature is observed during the months of April to July with 36ºC while the average lowest was observed during December and January months (winter months). The highest temperature may go up to 45ºC in summer. The average monthly pan evaporation of the area varies from 2.4 cm to 14.6 cm

On the basis of climate type, Odisha has been divided into ten agro-climatic zone. The normal rainfall of the state is 1451.2 mm. About 75% to 80% of rainfall is received during June to September. Floods, drought and cyclones occur almost every year with varying intensity.

Table 3.1 Salient features of Hirakud Reservoir

Latitude	21°29027.83″N	Design flood discharge	1500 000 cusec
Longitude	83°55031.04″E	Maximum water level (M.W.L.)	R.L. 192.024 m
River	Mahanadi	Full reservoir level (F.R.L.)	R.L. 192.02 m
Year of impoundment	1956	Minimum drawdown level (M.D.D.L.)	R.L. 179.83 m
Catchment area	84 788.94 km^2	Dead storage level (D.S.L.)	R.L. 152.40 m
Mean annual rainfall	1122.28 mm	Bed level	R.L. 150.87 m
Maximum annual rainfall	1928.42 mm	Gross storage capacity	8105 MCM
Mean annual run-off	3.313 M-ham	Live storage capacity	5843 MCM
Maximum annual run-off	9.09 M-ham	Dead storage capacity	2262 MCM
Minimum annual run-off	1.13 M-ham	Water spread area at F.R.L.	743 km^2
Mean annual run-off	3.313 M-ham	Water spread area at D.S.L.	274 km^2
Minimum annual run-off	1.13 M-ham	Available drawdown	12.192 m

3.4 Soil

Soil in the catchment area afine (44.11%) and clayey (0.74%) in character. The main soil types found in the catchment are red and yellow soils. The main upstream tributaries are Seonath, Jonk, Hasdeo, Mand and Ib. During the monsoon period (June–September), flood control is the main purpose of the dam, with the reservoir being used to meet water demands or irrigation, power generation, industrial needs, municipal water supply and ecological requirements during the post monsoon period and the reservoir is used to irrigate about 0.152 million ha as well as facilitating flood mitigation..

3.5. Agriculture

The crops grown in the sub-basin can be categorized as cereals (major crop), pulses, oilseeds, vegetables, fibres and spices and condiments. Among cereals, paddy is the major crop in the basin. Other cereals grown in the basin are wheat, small millets and maize. Pulses include moong, biri, khesari dal, gram and kulthi and oilseeds include groundnuts, soya-bean, sesame and mustard.

3.6 Optic satellite data used for delineating water spread area

LANDSAT-8

Landsat 8 is an American Earth observation satellite launched on 11 February 2013. It is the eighth satellite in the Landsat program, the seventh to reach orbit successfully. The Landsat 8 satellite payload consists of two sensors—the Operational Land Imager (OLI) and the Thermal Infrared Sensor (TIRS). These two sensors provide seasonal coverage of the

global landmass at a spatial resolution of 30 meters (visible, NIR, SWIR); 100 meters (thermal); and 15 meters (panchromatic). The Landsat 8 scene size is 185-km-cross-track-by-180-km-along-track. The nominal spacecraft altitude is 705 km.

Landsat 8 instruments represent an evolutionary advance in technology. OLI improves on past Landsat sensors using a technical approach demonstrated by a sensor flown on NASA's experimental EO-1 satellite. OLI is a push-broom sensor with a four-mirror telescope and 12-bit quantization. OLI collects data for visible, near infrared, and short wave infrared spectral bands as well as a panchromatic band. OLI provides two new spectral bands, one tailored especially for detecting cirrus clouds and the other for coastal zone observations. The OLI collects data for two new bands, a coastal/aerosol band (band 1) and a cirrus band (band 9), as well as the heritage Landsat multispectral bands. Additionally, the bandwidth has been refined for six of the heritage bands. The Thermal Instrument (TIRS) carries two additional thermal infrared bands.

SENTINEL-2

SENTINEL-2 is a European wide-swath, high-resolution, multi-spectral imaging mission. The Sentinel-2 mission comprises a constellation of two polar-orbiting satellites (Sentine-2A & 2B) placed in the same sun-synchronous orbit. The full mission specification of the twin satellites flying in the same orbit but phased at 180°, is designed to give a high revisit frequency of 5 days at the Equator. SENTINEL-2 carries an optical instrument payload (MSI-MultiSpectral Instrument))that samples 13 spectral bands: four bands at 10 m, six bands at 20 m and three bands at 60 m spatial resolution. The orbital swath width is 290 km.

The other details of Landsat8 and Sentinel-2 data used in this study are given in Table 3.2.

Table 3.2 Optic satellite data used for delineating water spread area.

Sl.No.	Satellite and Sensor	Date of Pass	Path/Row	Resolution	Reservoir Water Level (m)
1	LANDSAT-8 / OLI	29-Sep-18	141/45	30 m	191.84
2	Sentinel-2A / MSI	23-Oct-18	141/45	10m	191.38
3	Sentinel-2A / MSI	22-Nov-18	141/45	10m	190.82
4	Sentinel-2A / MSI	31-Jan-19	141/45	10m	189.78
5	Sentinel-2A / MSI	20-Feb-19	141/45	10m	189.20
6	LANDSAT-8 / OLI	25-Apr-19	141/45	30 m	186.75
7	LANDSAT-8 / OLI	11-May-19	141/45	30 m	185.48
8	LANDSAT-8 / OLI	27-May-19	141/45	30 m	184.22
9	LANDSAT-8 / OLI	12-Jun-19	141/45	30 m	183.51

3.7 Microwave satellite data used for delineating water spread area

In comparison to optical remote sensing, radar imaging has some advantages. As an active system, it is a day/night data acquisition system. Considering the behavior of electromagnetic waves in the range of RADAR wavelength, it can be seen that atmospheric characteristics such as cloud, light rain, haze. This makes microwave satellite data an all-

weather remote sensing system. One such microwave data known as SENTINEL-1 has been used in this study.

SENTINEL-1

The Sentinel-1 spacecraft, operating in near polar sun-synchronous orbit at 693 km height, provides accurate pointing knowledge and real time orbit determination, resulting in high geo-location accuracy of the SAR products. Sentinel-1 consolation has two satellites namely Sentinel-1A and Sentinel-1B.

Sentinel-1, SAR operates at a center frequency of 5.4 GHz, Inter-ferometric Wide swath(IW) mode data over Hirakud, adopted for this study, acquired in dual polarization (VV and VH). The IW mode is, providing a swath width of 250 km at a nominal ground resolution of 5 m X 20 m for single look data and offering enhanced image performance compared to the conventional Scan-SAR mode.

Level-1 data (swath-based SAR images) are available in two main categories: Single Look Complex imagery (SLC) and Ground Range Detected imagery (GRD). GRD products consist of focused SAR data having enhanced spatial resolution of 10m is used in this study. Other details of sentinel-1 data used are given in the Table No.3.3.

Table 3.3 Sentinel-1 satellite data used for delineating water spread area.

Sl. No.	Date of Acquisition	Satellite Mission	Polarization	Absolute orbit	Track of satellite pass	Reservoir Water Level (m)
1	19-Jun-2019	Sentinel-1A	VV & VH	27741	19	190.19
2	26-May-2019	Sentinel-1A	VV & VH	27391	19	189.23
3	14-May-2019	Sentinel-1A	VV & VH	27216	19	188.42
4	2-May-2019	Sentinel-1A	VV & VH	27041	19	187.41
5	20-Apr-2019	Sentinel-1A	VV & VH	26866	19	186.66
6	8-Apr-2019	Sentinel-1A	VV & VH	26691	19	186.17
7	27-Mar-2019	Sentinel-1A	VV & VH	26516	19	185.55
8	3-Mar-2019	Sentinel-1A	VV & VH	26166	19	184.80
9	26-Jan-2019	Sentinel-1A	VV & VH	25641	19	183.81
10	27-Nov-2018	Sentinel-1A	VV & VH	24766	19	182.86
11	10-Oct-2018	Sentinel-1A	VV & VH	24066	19	181.79

CHAPTER – 4
METHODOLOGY

4.1 Per-pixel Approach:

Water reflects most of the visible wavelengths, but the energy at the near-infrared (NIR) wavelength is almost absorbed by the water, thus providing a significant contrast between land and water in the NIR images. This contrast helps in extracting the water spread area of the reservoir. Different procedures have been adopted by many researchers for water body identification in wetland areas and reservoirs, each adopting the per-pixel based approach. Among these procedures, the band threshold approach is a relatively easy and valid method for identifying the water body. It has also been suggested that this per-pixel based approach can give acceptable estimates of the area of the water body if the NIR band is used. Therefore, in the per-pixel based approach, the band threshold technique would be adopted to extract the water pixels that correspond to various water levels of the reservoir. The following model equation has been used in the image processing software to delineate the water spread area of the reservoir. The adopted algorithm states that:

if

$P_{V\text{-}NIR} > T_{L\text{-}NIR}$ and $P_{V\text{-}NIR} < T_{H\text{-}NIR}$ then (4.1)

the pixel is in the water spread area, where $P_{V\text{-}NIR}$ is the pixel value in NIR band and $T_{L\text{-}NIR}$ and $T_{H\text{-}NIR}$ are the lower and higher thresholds for the NIR band.

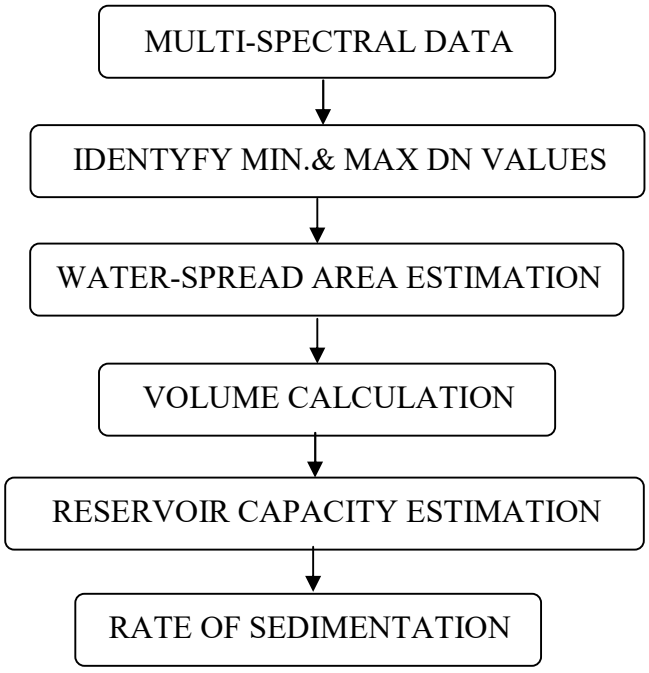

Figure 4.1 Flowchart showing the sequence of operations carried out for reservoir capacity estimation using the per-pixel classification approach.

4.2 Sub-pixel based approach:

The sub-pixel classifier uses the linear un-mixing technique, that allows in identifying the "material of interest" and determine its "material part fraction" or cover percentage, within a pixel.

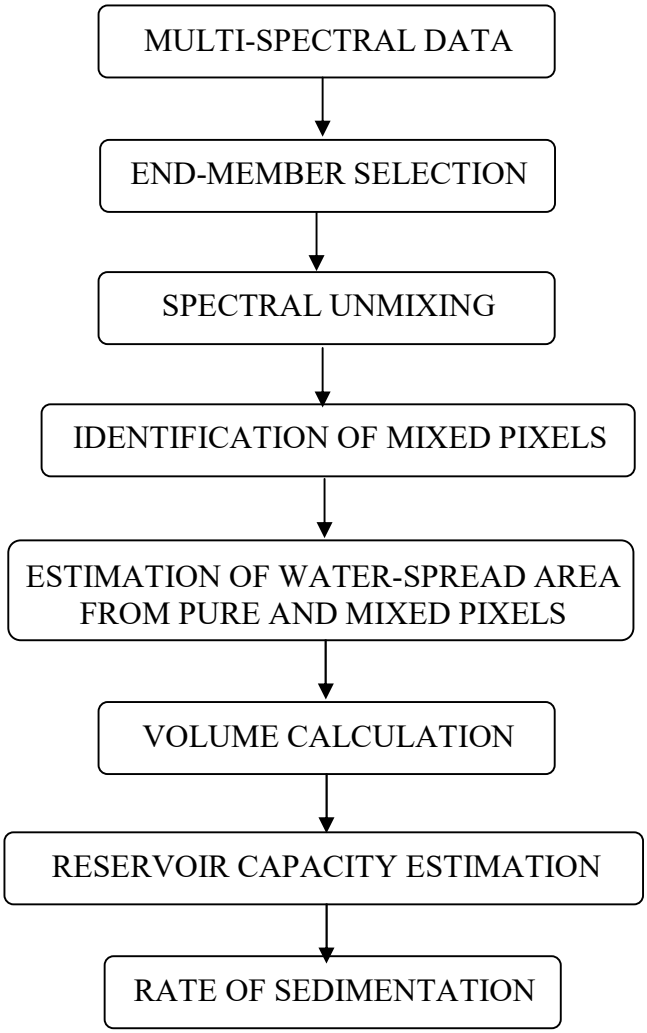

Figure 4.2 Flowchart showing the sequence of operations carried out for reservoir capacity estimation using the sub-pixel classification approach

Linear spectral un-mixing is an excellent approximation for calculating the abundance or fraction of an end-member in an image pixel. This soft classification technique aims at estimating the proportions of specific classes that occur within each pixel using linear mixing approach (Bryant 1994, Foody and Arora 1996, Arora and Foody 1997, Bajjouk et al. 1998, Aplin 2001). In this study the peripheral area of reservoir water-spread was estimated using linear spectral un-mixing approach.

The basic assumption of linear mixture model is that the measured reflectance of a pixel is the linear sum of the reflectance of the components that make up the pixel. The basic hypothesis is also that the image spectra are the result of mixtures of surface materials, shade and clouds, and that each of these components is linearly independent of the other (Quarmby et al. 1992, Borel et al. 1994, Van der Meer 1995, Bosdogianni et al. 1997, Atkinson 1997, Robert et al. 1998). Linear un-mixing also assumes that all the materials within the image

have sufficient spectral contrast to allow their separation. In soft classification, the estimated variables (the fractions or proportions of each land cover class) are continuous, ranging from 0 to 100 percent coverage within a pixel. Settle and Drake (1993) and Foody and Cox (1994), proposed a mathematical expression for linear spectral un-mixing. The theory behind this is the contribution of a series of end-members present within a pixel to its spectral signature. Hence, the spectral signature of a pixel would be derived from the sum of the products of the single spectrum of the end-members it contains, each weighted by a fraction plus a residue which would be explained by the following mathematical model:

$$R_i = \sum f_k R_{ik} + E_i \quad (4.2)$$

where $$\sum f_k = 1 \quad (4.3)$$

and $$0 \leq f_k \leq 1 \quad (4.4)$$

$i = 1, \ldots, m$ (number of spectral bands)
$k = 1, \ldots, n$ (number of end-members)
R_i = Spectral reflectance of band i of a pixel which contains one or more end-members
f_k = Proportion of end-member k within the pixel
R_{ik} = Known spectral reflectance of end-member k within the pixel on band i
E_i = Error for band i (Difference between the observed pixel reflectance (R_i) and the reflectance of that pixel computed from the model).

Equations 4.2 and 4.3 introduce the constraints that the sum of the fractions are equal to one and they are non-negative. To solve f_k, the following conditions must be satisfied: (i) selected end-members should be independent of each other, (ii) the number of end-members should be less than or equal to the spectral bands used, and (iii) selected spectral bands should not be highly correlated.

In this study, the linear spectral un-mixing is adopted based on the equations described below to segregate the actual information within a pixel of an image

$$\begin{aligned} R1 &= F_{water} * R1_{water} + F_{Veg} * R1_{Veg} + F_{Soil} * R1_{Soil} + \varepsilon 1 \\ R2 &= F_{water} * R2_{water} + F_{Veg} * R2_{Veg} + F_{Soil} * R2_{Soil} + \varepsilon 2 \\ R3 &= F_{water} * R3_{water} + F_{Veg} * R3_{Veg} + F_{Soil} * R3_{Soil} + \varepsilon 3 \end{aligned} \quad (4.5)$$

Where,

→R1, R2 and R3 represent the signal recorded at the satellite in the green, red and NIR bands of the LISS-III sensor.

→F_{water}, F_{Veg} and F_{Soil} are the fraction of the pixel covered by water, vegetation, and soil.

→$R1_{water}$, $R2_{water}$ and $R3_{water}$ represent the reflectance of water in each of the three spectral bands.

→$R1_{Veg}$, $R2_{Veg}$ and $R3_{Veg}$ represent the reflectance of vegetation in each of the three spectral bands.

→$R1_{Soil}$, $R2_{Soil}$ and $R3_{Soil}$ represent the reflectance of soil in each of the three spectral bands.

→ε1, ε2 and ε3 are the error components of band 1, 2, and 3.

The system of linear equations shown above can be solved by a least square solution which minimizes the sum of squares of errors.

4.2.1 Approaches to end-members selection:

End-members are pure pixels representing 100% or almost 100% of a single land cover class. A LMM is modelled as a linear function of spectral reflectance of end-members to derive the fractional area of land cover classes. The quality of the fraction images derived form spectral un-mixing depends on sufficient number and the proper selection of end-members. It is also believed that exact number of end-members is required to account for the spectral variability of the scene (Sabol et al 1992). Spectral un-mixing requires accurate, well-characterised end-members (Milton 1999). Improper choice of end members could result in erroneous computation of fractions of landcover classes present in an image. Therefore the concept of a spectral end-member is fundamental to the technique of spectral un-mixing. The identification and description of the physical and spectral properties of end-members is thus, of great importance in spectral un-mixing (Tompkins et al 1997, Milton 1999).

A number of approaches exist for the selection of end-members for use in spectral un-mixing. A few of them are:

1. Laboratory/field reflectance spectra (Boardman 1990).
2. Image pixels modelled as mixtures of library reflectance spectra (Smith et al 1990, Roberts et al 1993).
3. Automated techniques based on image transform (Full et al 1982, Boardman et al 1995).
4. n-Dimensional interactive visualization tools (Bateson and Curtiss 1996).
5. Based on the variability of image end-members - MESMA (Roberts et al 1998).
6. End-members based on class average RMSE (CAR) and end-member average RMSE (EAR), (Dennison and Roberts 2003).

Most of these techniques rely on image end-members. The advantage of the using image end-members in un-mixing is due to the fact that the end-members thus selected can be accounted for the variability of the scene and it is possible to model the image in a better fashion. A detailed description of some of the techniques that are widely used is given in the following sections.

4.2.3 N-Dimensional visualizer (NDV)

The sub-pixel based approach was applied to find out the proportion or fraction of water class that exits in the periphery pixels of the reservoir. The first step executed in the sub-pixel approach was, selection of end-members. In general the border pixels of a reservoir may contain any combination and proportions of water, vegetation and soil classes, therefore these three classes were chosen to collect the end-members. “N-Dimensional visualizer” (NDV) and “Pixel Purity Index” (PPI) functions were used to identify the end-members. The identified end-member spectra were supplied as input to the linear mixture model (LMM) approach. The out put of the LMM delivers number of fractions images as that of the end-members selected/feeded into the model. The number of end-members selected should be less than or equal to the total number availability of bands in an image. In this study only three end-members have been used and hence the output of the model run would contain three end-member images known as water, soil and vegetation fraction images and an error image.

4.2.4 Pixel Purity Index (PPI) approach

Pixel Purity Index (PPI) is another technique for the delineation of pure pixel, which involves repeatedly projecting n-Dimensional scatter plots onto a random unit vector. The highest and lowest reflectance pixels of the projection are scored including any other pixels located within a specified standard deviation range (i.e., the designated threshold value). Pixels with extreme values are scored most often and represent the corners (i.e., vertices) of the multi-dimensional cloud of data points (Boardman 1993). By understanding all of the spectral features that lie at the vertices (i.e., 'pure' pixels) of the multi-dimensional cloud, it is possible to understand internal mixtures of those features. PPI allows for spatial data reduction. The pixels in the image that represent the 'most pure' spectral signatures are identified and subset from the mass majority of pixels representing mixed pixels. The most spectrally pure pixels typically correspond to mixing end-member. The PPI is typically run on MNF (Maximum Noise Transform) image data suggested by Green et al 1988, which determines the intrinsic dimensionality of the image data segregates the noise effect and reduces computational requirements for use in subsequent processing of the image data (Boardman and Kruse 1994).

The result of the application of PPI is a PPI score image with bright and dark pixels, each pixel having a distinct score. The PPI score indicates the purity of the pixel. A pixel with higher PPI score indicates higher purity and hence, appears brighter in the image. Pixel with lower score is less 'spectrally pure' and appears darker in the PPI image. Pixels with higher PPI score are usually taken as end-members for use in spectral un-mixing (Boardman 1993).

4.3 Super-resolution Approach:

In this work, super resolution mapping would be achieved by integrating linear spectral unmixing and hopfield neural network approach. Hopfield neural network (HNN) is a feed-forward neural networks, each neuron is modeled using input and a sigmoidal activation function. It is fully connected recurrent network. The Hopfield network can be used for energy minimization problems if the weights and biases are arranged such that they describe an energy function, with the minimum of energy occurring at the stable state of the network.

Mapping the spatial distribution of class components within each pixel is formulated as a constraint satisfaction problem with an optimal solution determined by the minimum of the cost function. From the multi-spectral satellite images, a set of proportion images for each land cover class is obtained by the linear spectral unmixing technique. The super resolved map for the multispectral images are obtained from the fraction image and by using the neural network technique.

Each pixel in the input image to the neural network is to be processed by a set of 5 x 5 (25) neurons. The network for each pixel processing is constructed with 25 neurons, since a zoom factor of 5 is adopted. The LANDSAT-8/OLI image of 30 m resolution is classified and enhanced to a 6m super resolved map. The SENTINEL-2A data which have 10m resolution was enhanced to 5m by processing 2 x2 neurons.

The neurons are given an initial value as follows: If a pixel has an area proportion for a particular landcover class as 100%, all neurons are given a value of 0.55. Similarly, if a pixel has an area proportion for a particular landcover class as 50%, 13 neurons are given a value

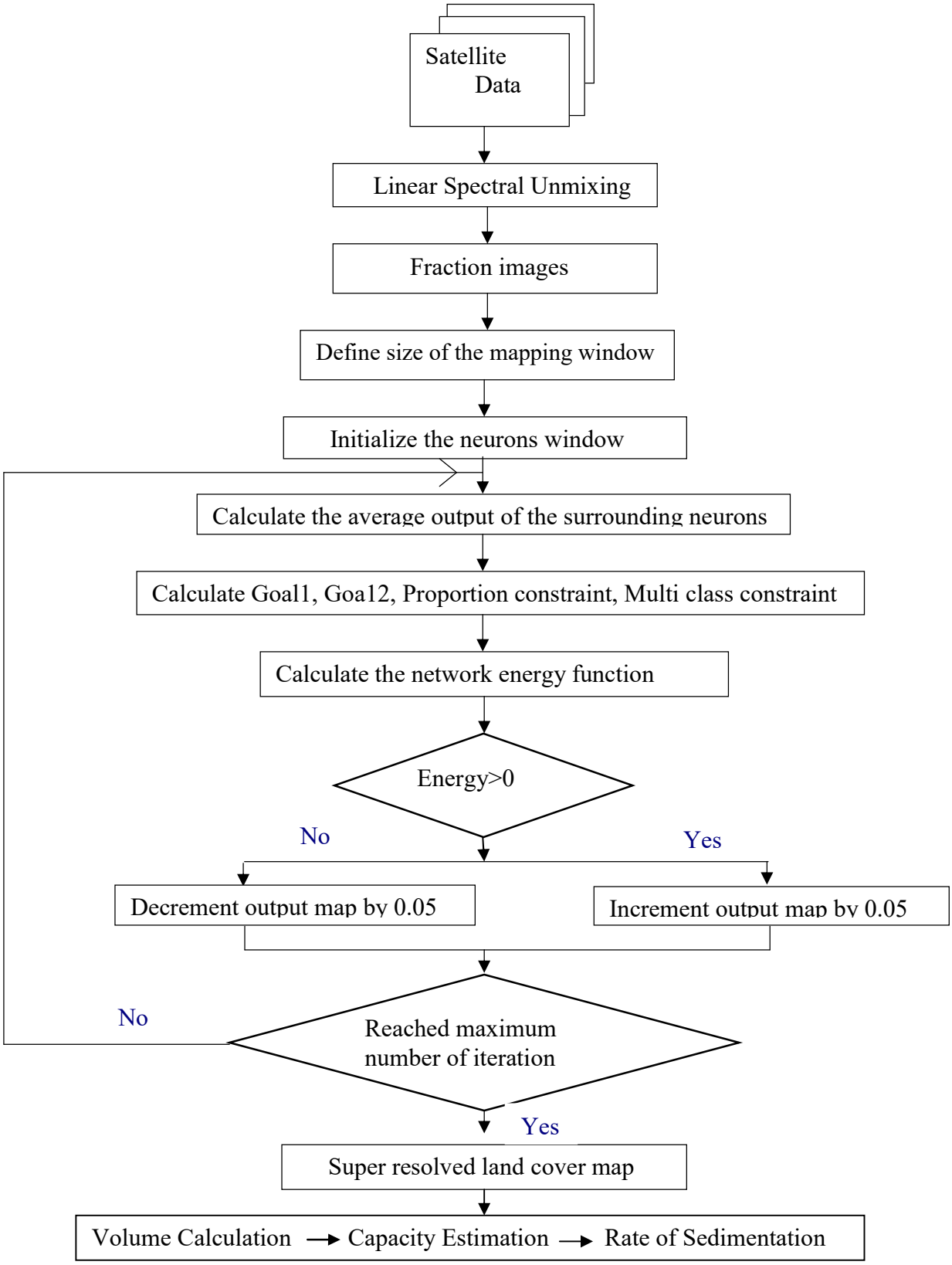

Figure 4.3 Flowchart showing the sequence of operations carried out for reservoir capacity estimation using the super resolution mapping approach.

of 0.55 and 12 neurons are given a value of 0.45. The concept of spatial order within and outside a pixel is the basis for determining the energy of the network. The point at which minimum energy occurs is the stable state of the network. The neuron outputs at this point determine the best accurate map of the given image. The network energy function given in Equation (4.6) based on the goal and constraints of the sub-pixel level mapping task is:

$$E = -\sum\sum(k1G1 + k2G2 + k3P + k4M) \tag{4.6}$$

where k1, k2, k3 – constants weighting the various energy parameters taken a value = 1
G1 and G2 – output values for neuron of the two objective (or) goal functions
P – output value for neuron of the proportion constraint
M – output value of the neuron for multi-class constraint,

$$M = \left(\sum_{j=1}^{Total\ class} avg_{kij}\right) - 1,$$

where avg_{kij} is average output of j^{th} class for sub-pixel at position (i,j).
The first goal function given in Equation (4.7) is aimed to increase the output of the central neuron to 1 if the average output of the surrounding eight neurons was greater than 0.5.

$$G1(i,j) = \Big(\text{floor}\big(1 + \tanh(\text{average}(\text{surrounding eight neurons output}) - 0.5)\big)\Big) \setminus \big(\text{neuronoutput}(i,j) - 1.0\big); \tag{4.7}$$

If the averaged output of the neighboring neurons is less than 0.5, the goal function evaluates to 0, and has no effect on the energy function. If the averaged output is greater than 0.5, the goal function evaluates to 1 and the neuron output controls the magnitude of the negative gradient output, with only neuron output of 1 producing a zero gradient. A negative gradient is required to increase the neuron output, when the output = 0 and the mean of surrounding 8 neurons is greater than 0.5.

The second goal function given in Equation (4.8) aims to decrease the output of the central neuron to 0, given that the average output of the surrounding eight neurons was less than 0.5.

$$G2(i,j) = (1 - \text{floor}(1 + \tanh(\text{average}(\text{surrounding eight neurons output}) - 0.5))) * \text{neuronoutput}(i,j); \tag{4.8}$$

The *tanh* function evaluates to 0 if the averaged output of the neighboring neurons is more than 0.5. If it is less than 0.5, the function evaluates to 1 and the central neuron output controls the magnitude of the positive gradient output. If the neuron output = 0, the second goal function produces a zero gradient.

$$P = floor((1 + \tanh(neuronoutput(i,j) - 0.5))) - p(i,j); \tag{4.9}$$

where p(i,j) is the estimated proportion
A positive gradient is required to decrease the neuron output when the neuron output =1 and the average of the surrounding 8 neurons is less than 0.5.
When neuron output=1 and average of surrounding 8 neurons >0.5, G1=0
When neuron output=0 and average of surrounding 8 neurons<0.5, G2=0
Energy = G1 + G2 = 0

This satisfies the objective of the super resolution mapping task, while also forcing the neuron output to either 0 or 1 to produce a bipolar map of the given image. The proportion

constraint is used to check whether the area proportion estimate of each pixel of the input image is maintained during the energy minimization process (super-resolution mapping task). A positive P value (4.9) is produced if proportion estimate exceeds the actual value and a negative P value is produced if proportion estimate is less than the actual value. When the proportion estimate is equal to the actual initial value, P=0 and E=0. The super resolved fraction or proportion image is obtained for each class. The super-resolved map gives the information on the spatial distribution of classes within the pixel, which is typical of the heterogeneous nature of the earth.

4.3 Microwave data

4.3.1 Pre-processing of Sentinel 1-SAR data

A standard generic workflow (Figure 4.4) to preprocess the Sentinel-1 GRD data is described below. The work flow was created in order to be used within the Sentinel application platform (SNAP), a common architecture for all Sentinel satellite toolboxes. The preprocessing steps are designed to reduce the error propagation in the subsequent processes. Pre-processing steps such as Applying orbit file, thermal noise removal, calibration, Speckle filtering and geo-metric resampling were carried to analyze the SAR data. These steps are explained below.

Apply Orbit File

Orbit state vectors, contained within the metadata information of SAR products, are generally not accurate (Federico Filipponi, 2019). The precise orbits of satellites are determined after several days and are available days-to-weeks after the generation of the product. The operation of applying a precise orbit available in SNAP allows the automatic download and update of the orbit state vectors for each SAR scene in its product metadata, providing an accurate satellite position and velocity information.

Thermal Noise Removal

Sentinel-1 image intensity is disturbed by additive thermal noise, particularly in the cross-polarization channel (Park, J.W., et al., 2017). Thermal noise removal reduces noise effects in the inter-sub-swath texture, in particular, normalizing the backscatter signal within the entire Sentinel-1 scene and resulting in reduced discontinuities between sub-swaths for scenes in multi-swath acquisition modes. The thermal noise removal operator available in SNAP for Sentinel-1 data can also re-introduce the noise signal that could have been removed during level-1 product generation, and update product annotations to allow for re-application of the correction. Sentinel-1 level-1 products provide a noise look-up table (LUT), provided in linear power, for each measurement data set and used to derive calibrated noise profiles matching the calibrated GRD data (SNAP Software, 2019).

Calibration

Calibration is the procedure that converts digital pixel values to radiometrically calibrated SAR backscatter. The information required to apply the calibration equation is included within the Sentinel-1 GRD product; specifically, a calibration vector included as an annotation in the product allows simple conversion of image intensity values into sigma nought values. The calibration reverses the scaling factor applied during level-1 product

generation, and applies a constant offset and a range-dependent gain, including the absolute calibration constant.

In the proposed preprocessing workflow, a LUT to produce sigma nought values is proposed, in order to generate radiometrically calibrated SAR backscatter with respect to the nominally horizontal plane. Sigma specifies the strength of reflection in terms of the geometric cross section of a conducting sphere, and represents the radar cross section of a

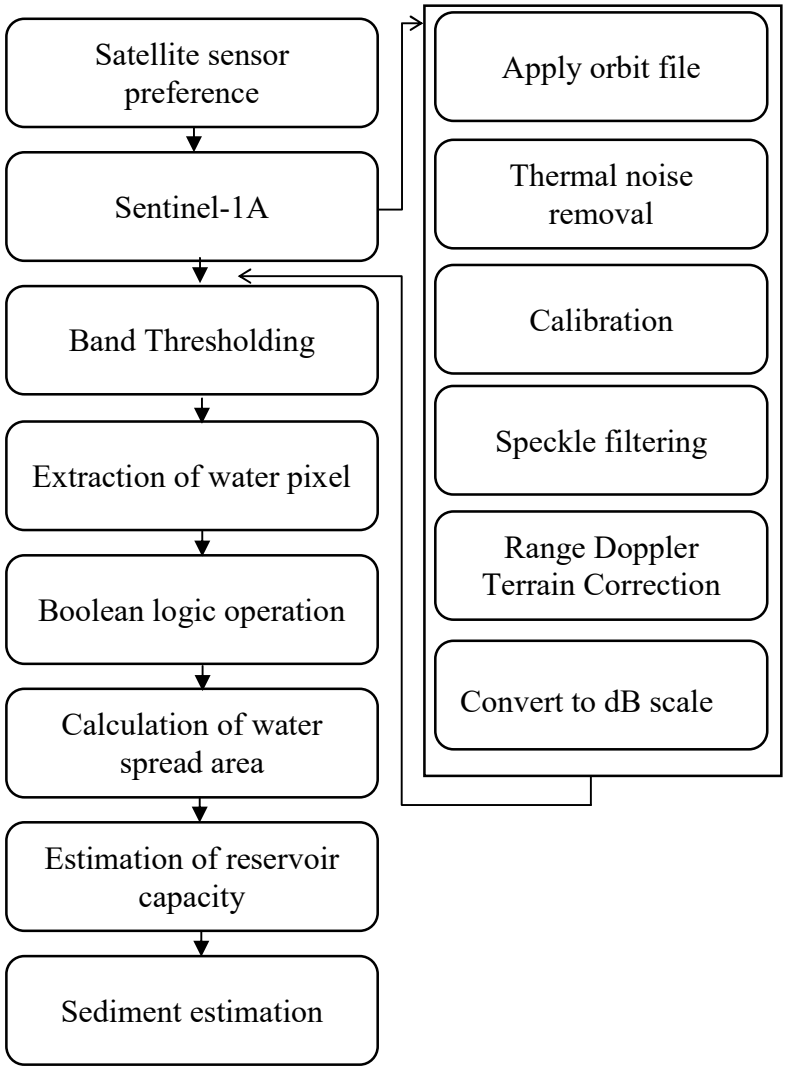

Figure 4.4 Flowchart showing the sequence of operations carried out for reservoir capacity estimation using the microwave data (Sentinel-1A).

distributed target over that expected from an area of one square meter. The sigma nought has a significant variation with the incidence angle, wavelength, and polarization, as well as with properties of the scattering surface.

Speckle Filtering

Speckle, appearing in SAR images as granular noise, is due to the interference of waves reflected from many elementary scatterers (Lee, J.S., et al, 1994). Speckle filtering is a procedure to increase image quality by reducing speckle. When such a procedure is done at

an early processing stage of SAR data, speckle is not propagated in ongoing processes (i.e., terrain correction or conversion to dB). Speckle filtering is not advisable when there is an interest in the identification of small spatial structures or image texture, since it might remove such information. The refined Lee filter has been found to be superior, with respect to other single product speckle filters, for visual interpretation, because of its ability to preserve edges, linear features, and point target and texture information (Lee, J.S., et al, 1994). More recently, multitemporal speckle filters have been developed to reduce speckle, taking advantages from multiple SAR observations in time. The proposed preprocessing workflow includes a speckle filtering step, which could be skipped by selecting 'None' as the filter type. Currently, one of the following filters is available in the SNAP single product speckle filter operator: 'Boxcar', 'Median', 'Frost', 'Gamma Map', 'Lee', 'Refined Lee', 'Lee Sigma', 'IDAN'.

Range Doppler Terrain Correction

SAR data are generally sensed with a varying viewing angle greater than 0 degrees, resulting in images with some distortion related to side-looking geometry. Terrain corrections are intended to compensate for these distortions so that the geometric representation of the image will be as close as possible to the real world. Range Doppler terrain correction is a correction of geometric distortions caused by topography, such as foreshortening and shadows, using a digital elevation model to correct the location of each pixel. The range Doppler terrain correction operator available in SNAP implements the Range Doppler ortho-rectification method for geocoding SAR scenes from images in radar geometry. It makes use of available orbit state vector information in the metadata, the radar timing annotations, and the slant to ground range conversion parameters together with the reference digital elevation model data to derive the precise geo-location information (SNAP Software, 2019). The target Coordinate Reference System (CRS) can be selected and optionally set to match the UTM zone of the overlaying Sentinel-2 granules.

Conversion to dB scale

As a last step of the preprocessing workflow, the unitless backscatter coefficient is converted to dB using a logarithmic transformation.

After SAR image is preprocessed and its histogram analyzed, threshold value range is fixed to extract the water pixels from the SAR image using mask manager feature of SNAP.

4.4. Computation of volume between successive water levels

The water-spread area estimated using per-pixel approach was used as an input in the volume estimation formula to find out the volume at different water levels of the reservoir. Traditionally the reservoir volume between two consecutive reservoir water levels, has been computed using the Prismoidal formula, the Simpson formula and the Trapezoidal formulae (Patra 2001). Of these, the Prismoidal formula has been most widely used for computation of volume (Rao *et al.* 1985, Goel and Jain 1996, Morris and Fan 1998, Rathore 2006). In this study, the volume between two consecutive reservoir water levels was computed using the following Prismoidal formula.

Prismoidal Formula : $V = H/3(A1 + A2 + \sqrt{A1*A2})$ (4.10)

Where V is the volume between two consecutive water levels. A1 and A2 are the water-spread area at the reservoir water level 1 and 2 respectively and H is the difference between these two water levels.

4.5 Computation of storage capacity of the reservoir

The volume computed at different water levels (i.e from Minimum Draw Down Level to Full Reservoir Level) was added up to calculate the live storage capacity of the reservoir. The difference between any two capacity survey reveals the amount of sediment deposited in the reservoir.

CHAPTER-5
RESULTS AND DISCUSSIONS

This chapter deliberates on the observations recorded while performing the experiments related to the role of multi-spectral images and multi-spectral information in reservoir water-spread area and reservoir capacity estimation. This chapter is divided into Part-I and Part-II. Part-I & II elaborates the assessment of rate sedimentation in Hirakud reservoir using optic and microwave satellite data respectively. In Part-I results of three different methodologies namely per-pixel, sub-pixel and super resolution approaches have been analyzed and effort has been made to identify the best methodology among the three for the estimation of rate of sedimentation in Hirakud reservoir. In the first section, the role and implications of the per-pixel classification approach in estimating the reservoir water-spread areas and in turn the rate of sedimentation are discussed. In the second and third sections results obtained using the sub-pixel and super resolution approaches are elaborated. Validation of per-pixel, sub-pixel and super resolution approaches are explained in the fourth section.

The optical satellite system have many advantages such as high spatial resolution and the ability to analysis various earth surface features using combination of spectral data. However, the images obtained from optic sensors is dormant if the area of interest is covered by clouds. Hirakud reservoir is often affected by cyclonic storms, in such situations it is difficult to get the clear optic satellite data. To overcome such situations the microwave data is used in this study and the earth surface details are obtained. Part-II has been devoted for the analysis of results obtained using microwave satellite data.

Part-I : Assessment of sedimentation using optic satellite data:

In the remote sensing system mostly optic satellite data is used due to its many advantages such as high spatial resolution and the ability to analysis the earth objects using different spectral data. The optic satellites namely Lansat-8 and Sentinel-2 have been used in this study. The spatial and spectral details of these satellites used for classification of water spread area are given in the Chapter-3 (Data Used). For all the three approaches (per-pixel, sub-pixel and super resolution), the same satellite images have been used and water spread areas have been interpreted. The analysis are discussed in the following sections.

The image data used in this study was recorded by the Landsat-8 satellite and its sensor Operational Land Imager (OLI). The OLI (Path/Row: 141/ 45) provides information of the land surface though 8 bands with a spatial resolution of 30m. Out of these eight bands, the 3^{rd} 4^{th} and 5^{th} bands which are known as Green, Red and Near Infra-red (NIR) bands have been used in this study. These three bands spectral resolutions are 0.525-0.600 μm, 0.630-0.680 μm and 0.85-0.88 μm respectively.

The Sentinel-2 satellite with the sensor namely Multi-Spectral Instrument (MSI) provides the data in thirteen bands, band 8 (NIR), with a spatial resolution of 10m having central wavelength 0.832μm has been used for extracting the water pixels. OLI sensor have 12 bit (i.e 2^{12}) radio-metric resolution, hence the pixels or the image captured by these sensor contain, Digital Number ranging from 0 to 4095. Whereas, the OLI instrument acquires measurement in 12 bits. These measurements are converted to reflectance and stored as 16 bit integers, which have values ranges from 0 to 65,535. The Hirakud reservoir pertaining to

Sentinel-2 data is covered in four different path. Sentinel-2 satellite captures single day Hirakud reservoirs water-spread area in four different scenes. Therefore, these four pieces of images were down-loaded and mosaic operation was performed. This process was carried for all the Sentinel-2 image data used in this study.

5.1 Estimation of rate of sedimentation by per-pixel classification approach

Nine water levels varying from 191.84 m to 183.51 m of the reservoir were selected based on the availability of cloud-free satellite data to estimate the water spread of the reservoir for the period 2018-19. The impoundment FRL and MDDL of the reservoir were 192.02 m and 179.83 m respectively. To extract the water pixels from the images using the per-pixel approach, the algorithm presented in Equation (1) described in the methodology was used. This algorithm needs separate minimum and maximum threshold DN values from the NIR band for the nine satellite images used in the study. With the help of the said algorithm, the pixels which contain the DN numbers between the identified minimum and maximum threshold values were labeled as water pixels. The locations of these pixels in the water spread area were also verified and showed that the pixels with low DN value were positioned in the deeper and central portion of the water spread area of the reservoir. The extracted minimum DN values are 336, 139, 272, 220, 231, 340, 270, 274 and 357 for the images pertaining to January, February, April, May (month have two dates of data), June, October, November, and September respectively. The lower (139) and higher (357) DN values can be attributed to the irradiance of the water body during the winter and summer seasons of the study area. The examination of DN values of the water body shows that the pixel value increases towards the boundary of the water body and the border pixels have the maximum DN value. In selecting the maximum value of the water spread area, one must examine the pixels along the boundary of the reservoir. The extracted maximum pixel values are 900,901,930,988,1160,600,870 and 512 for the images pertaining to the months of January, February, April, May, June, October, November and September respectively. The pixel values of 274 and 340 pertain to the winter (November) and summer (June) seasons of the study area.

The total number of water pixels that were extracted was multiplied by the area 30m x 30m (for Landsat-8 data) & 10m x 10m (for Sentinel-2 data) of a single-pixel to compute the water spread area occupied by a particular water level. The same technique was adopted to convert the extracted water pixels into the water spread area in all nine images used in this study. The satellite image data for various water levels and the extracted water spread areas are shown in Figure 5.1 and 5.2 respectively.

The water spread area extracted using the per-pixel classification approach for all the nine water levels are provided in Table 5.1. The cloud free digital image data that could be captured by the satellites for the year 2018-19, were between the water level 183.51m and 191.84m. Due to presence of cloud, optic satellite data was not available below 183.51 m to MDDL (179.83 m) and above 191.84 m to FRL (192.02 m). The live storage capacity of the reservoir ranges from 179.83 m (MDDL) to 192.02 m (FRL).

Table 5.1. Satellite data derived water spread area using per-pixel classification approach.

Sl.No.	Satellite and Sensor	Date of Pass	Reservoir Water Level (m)	Interpreted water spread area from the satellite data (Ha)
1	LANDSAT-8 / OLI	29-Sep-18	191.84	59881.34
2	Sentinel-2A / MSI	23-Oct-18	191.38	57458.91
3	Sentinel-2A / MSI	22-Nov-18	190.82	54605.93
4	Sentinel-2A / MSI	31-Jan-19	189.78	49587.44
5	Sentinel-2A / MSI	20-Feb-19	189.20	46946.70
6	LANDSAT-8 / OLI	25-Apr-19	186.75	37040.46
7	LANDSAT-8 / OLI	11-May-19	185.48	32700.02
8	LANDSAT-8 / OLI	27-May-19	184.22	28929.94
9	LANDSAT-8 / OLI	12-Jun-19	183.51	27040.78

A second order polynomial equation (6.1) was fitted for the water spread area estimated from the satellite data using per-pixel classification approach and the revised water spread areas at regular intervals were calculated and given in Table 5.2.

Water Spread Area in hectare = $(168.197 * L^2) - (59190.3 * L) + 5224864$ (6.1)

Where L = Reservoir water level in meter

The above said procedures such as fitting of polynomial equation and arriving the water spread area for the regular intervals have been adopted for all the three sections which deals the sub-pixel, super-resolution approaches and microwave satellite data methodology to estimate the rate of sedimentation.

Table 5.2 Water spread area estimated at regular intervals using per-pixel classification approach.

Sl.No.	Reservoir elevation above M.S.L (m)	Water-spread area estimated using per-pixel approach (Ha)
1.	192.02 (FRL)	60849 (608.49 Mm^2)
2.	191	55511
3.	190	50619
4.	189	46062
5.	188	41842
6.	187	37959
7.	186	34412
8.	185	31201
9.	184	28326
10.	183	25788
11.	182	23587
12	181	21722
13.	180	20193
14.	179.83 (MDDL)	19966

Most of the Indian reservoirs utilize the prismoidal formula to estimate the volume between two water levels during the impoundment survey. Therefore, in this study also, the prismoidal formula was used to calculate the volume arises between different water levels used in the analysis.

The revised water-spread areas that were estimated using per-pixel classification approach at regular intervals were utilized to compute the volumes between the MDDL and FRL. The volumes thus calculated have been added up to find out the cumulative live storage capacity of the reservoir. The estimated cumulative live storage capacity of the Hirakud reservoir, according to the per-pixel classification approach, for the period 2018-19 was 4419.60 M.cum. Hirakud reservoir's original live storage capacity during 1956 was 5842.88 M.cum. The difference between the 1956 live capacity and the present live capacity reveals the amount of sediment deposited during 63 years of operation of the reservoir, which is estimated at 1423.28 M.cum. Therefore, from the per-pixel approach calculations it is assessed that 1423.28 M.Cum of sediment has been deposited in the Hirakud reservoir during the period 1957 to 2019. Hence, the rate of sedimentation in the live storage capacity of Hirakud reservoir is estimated at 22.56 M.Cum/year. The calculations are given in Table 5.3.

Table 5.3 Reservoir capacity estimation using per-pixel classification approach

Sl.No.	Reservoir elevation above M.S.L (m)	Water-spread area estimated using per-pixel approach (Ha)	Cumulative Capacity (Ha-m)
1.	192.02 (FRL)	60849 (608.49 Mm^2)	441960 (4419.60 Mm^3)
2.	191	55511	382641
3.	190	50619	329595
4.	189	46062	281277
5.	188	41842	237342
6.	187	37959	197457
7.	186	34412	161286
8.	185	31201	128493
9.	184	28326	98741
10.	183	25788	71693
11.	182	23587	47014
12	181	21722	24366
13.	180	20193	3413.5
14.	179.83 (MDDL)	19966	0

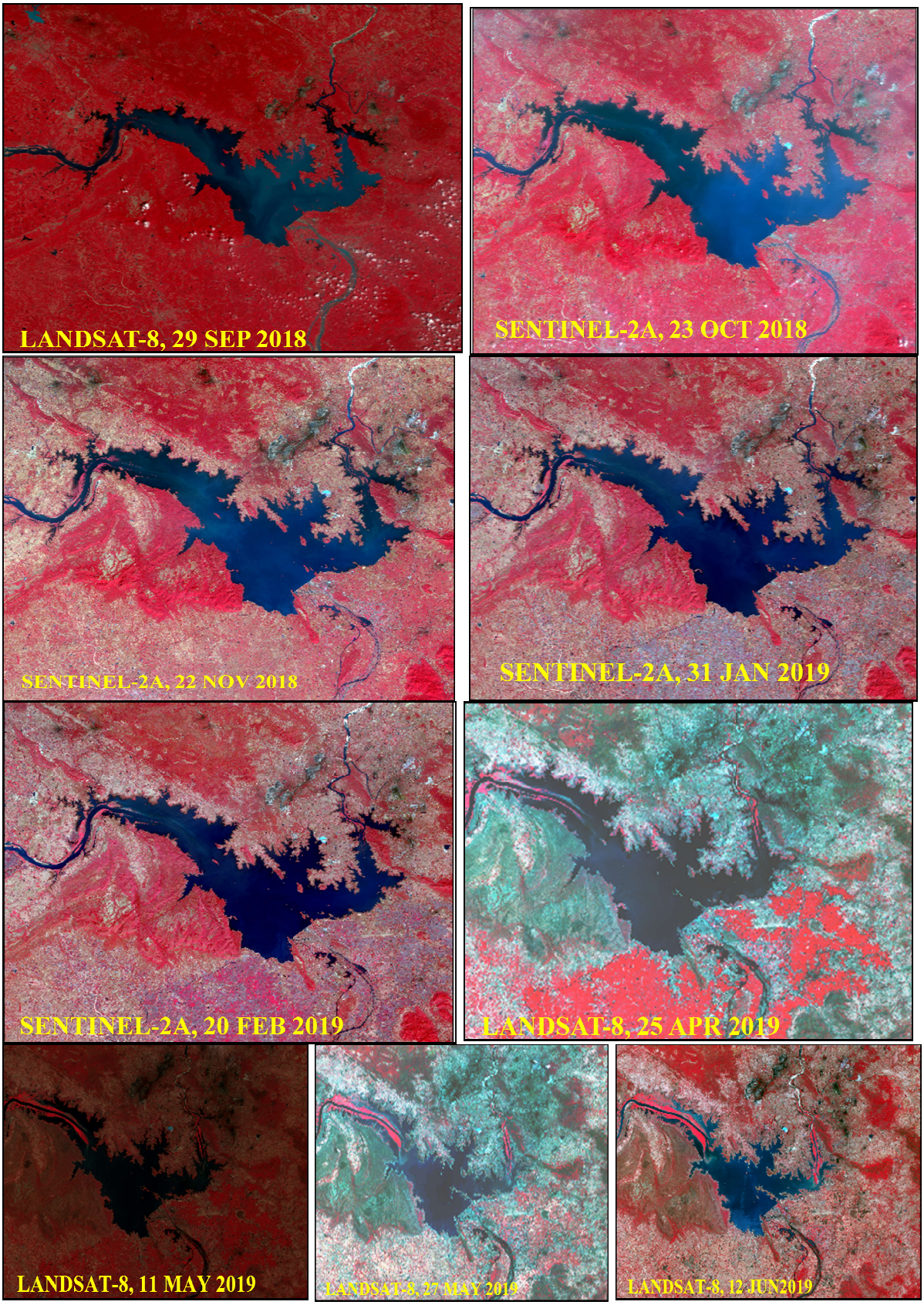

Fig 5.1 Satellite data set used for the period 2018-2019.

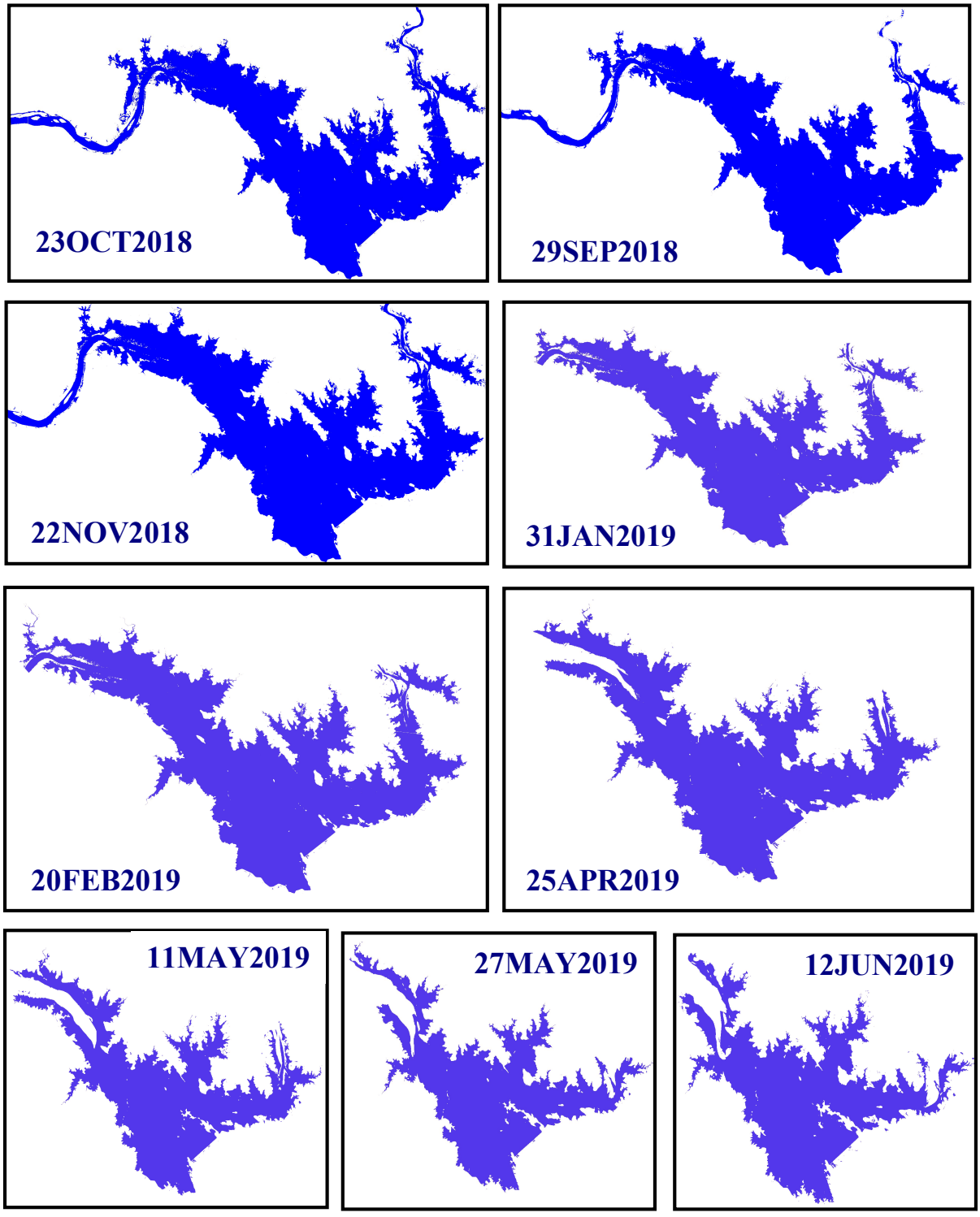

Fig.5.2 Per-pixel classified water-spread area from the multi-date satellite for the period 2018-19

5.2 Estimation of rate of sedimentation by sub-pixel classification approach

The per-pixel approach produces single classification out-put, which contains information about all the landusue/landcover classes in the study area. Whereas, in the Sub-Pixel Classification (SPC) approach, the classification out-put produces more than one image, concurrence to the number of end-members used. End-members are the pure pixels of different land classes used in the classification approach. The out-put images of SPC are known as fraction images. These fraction images contain a wealth of information about different end-members used in the model. In this, study the end-members from the classes such as water, vegetation and soil were used. Therefore, the SPC out-put had three fraction images known as water, vegetation and soil fraction images, i.e each fraction image corresponds to a single land cover only. The pixels in the water fraction image provide information only on the proportion or amount of water it contains. Likewise the vegetation and soil fraction images provide information on the proportions of the respective classes only. (The residual error created by the model is depicted by the error image). However, in this study the interest is only to know about, the amount of water present in every water level of the reservoir, hence only the water fraction image has been used. The value of the pixels in the fraction image ranges from 0 to 1. A pixel from the water fraction image having a value of 0 indicates that there is no water at all in that pixel, whereas a pixel having a value of 0.3 indicates that 30% of the area of the pixel is occupied by water. While a pixel value of 1 indicates that 100% of the area of the pixel is occupied by water (i.e the pixel is fully occupied by water). Therefore, in the LANDSAT8/OLI image data (which contain a spatial resolution of 30m), a pixel having a value of 0.7, the area of water occupied by that pixel is 630 m^2 (0.7 x 30m x 30m). In the case of SENTINEL-2 data (which contain a spatial resolution of 10m) for a pixel having a value of 0.5, the water area occupied by that pixel is 50 m^2 (0.5 x 10m x 10m).

End-members are the required input to run the sub-pixel classification model. In this study the end-members were identified using n-Dimensional Visualizer (NDV) and Pixel Purity Index (PPI). Each and every image pertaining to Hirakud reservoir used in this study produced many number of end-members. NDV and PPI allow the analyst to view the spectral characteristics of these pixels in multiple dimensions. Interactively, the analyst can identify the pixels with their corresponding DN values in various wavelength bands and then identify their locations on the image. For instance, the water end-members show very low, moderate and high DN value in the NIR, Red and Green band wavelengths. Among the NDV and PPI produced pixels, the pixel which has the lowest DN in NIR and highest value in red and green bands have been selected as water end-member. In the case of vegetation end-member green, red and NIR bands show moderate, low and very high DN value. The end-member of the vegetation class has been selected in the same order as the spectral characteristic of the class, i.e the pixel which has moderate DN value in the green band, very low DN value in the red band and very high DN value in the NIR band. The end-member of the soil class has been selected based on the site characteristics, i.e the pixel which has lowest DN value in green band and higher DN value in the red and NIR band. As explained above the selected end-members were used as input in the SPC model and three different fraction images were obtained as output. The sub-pixel classified images pertaining to Hirakud reservoir for three different water levels (near FRL, moderate water level and near MDDL) are shown in Figure 5.3 to 5.5. From the three fraction images the water fraction image alone has been utilized to estimate the water-spread area pertaining to every water level of the reservoir.

Here it is worth mentioning that, a pixel containing 65% of water may be labelled as containing 100% of water by the per-pixel approach. Thus the water-spread area is over estimated. Conversely, in the per-pixel classification approach the pixel containing 40% of water may not be considered as a water pixel. Hence, the water-spread area is under estimated. Such errors due to over estimation or under estimation do not occur in the SPC approach. Thus, the SPC approach reduces the error imposed by the per-pixel classification approach.

All the nine water fraction images of the Hirakud reservoir were examined and found that the inner portion of water-spread area contains pixel value of 1. Whereas, the peripheral or border pixels contain proportions of value ranging from 0.99 to 0.1. It was ascertained that a small number of the border pixels contain water spread area less than 10%. Hence, a threshold value of 10% was selected and the pixels containing value of less 0.1 were omitted from the analysis. The pixels which have value of 1 to 0.1 were used in the estimation of water-spread area. The pixels representing the peripheral portion of the reservoir, which have value of 0.99 to 0.1 were isolated from the water-fraction image and the area covered by water in these peripheral/border pixels were estimated. The number of pixels that contain 100% water were also determined. By summing the area occupied by these two types of pixels, the total water spread area corresponding to a particular water level of the reservoir was computed. This exercise was carried out for all the nine images used in the study. Thus, the water spread areas of all the nine water levels were computed using the sub-pixel classification approach for the period 2018-19. The interpreted water spread areas using sub-pixel classification approach is given in Table 5.4.

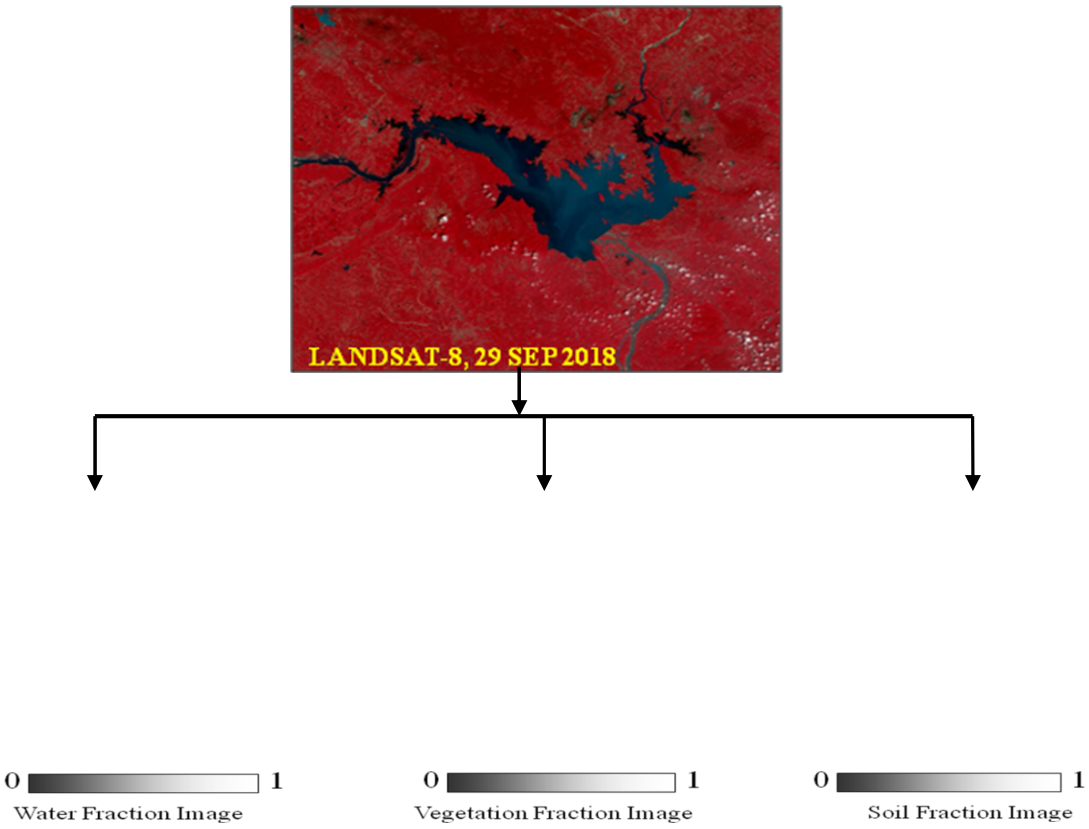

Fig.5.3. Sub-pixel classified output of Hirakud Reservoir for the water level 191.84

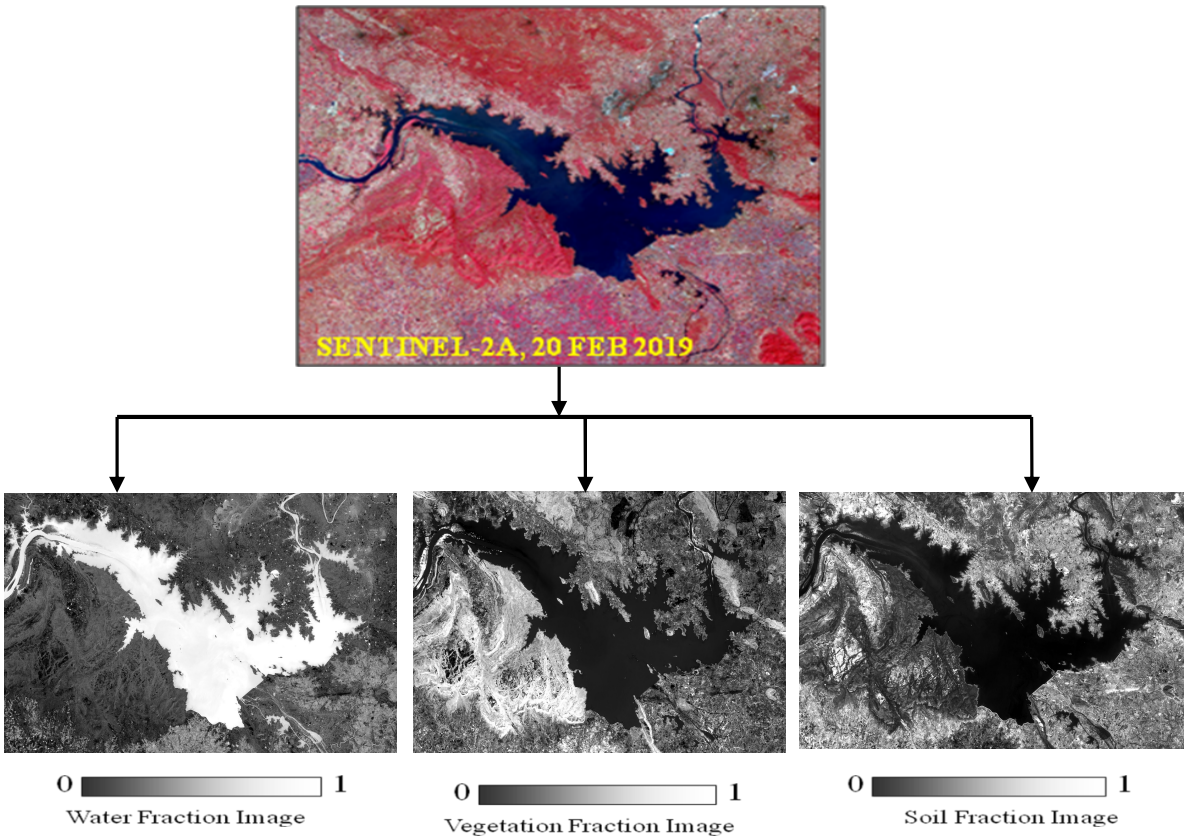

Fig.5.4. Sub-pixel classified output of Hirakud reservoir for the water level 189.20 m

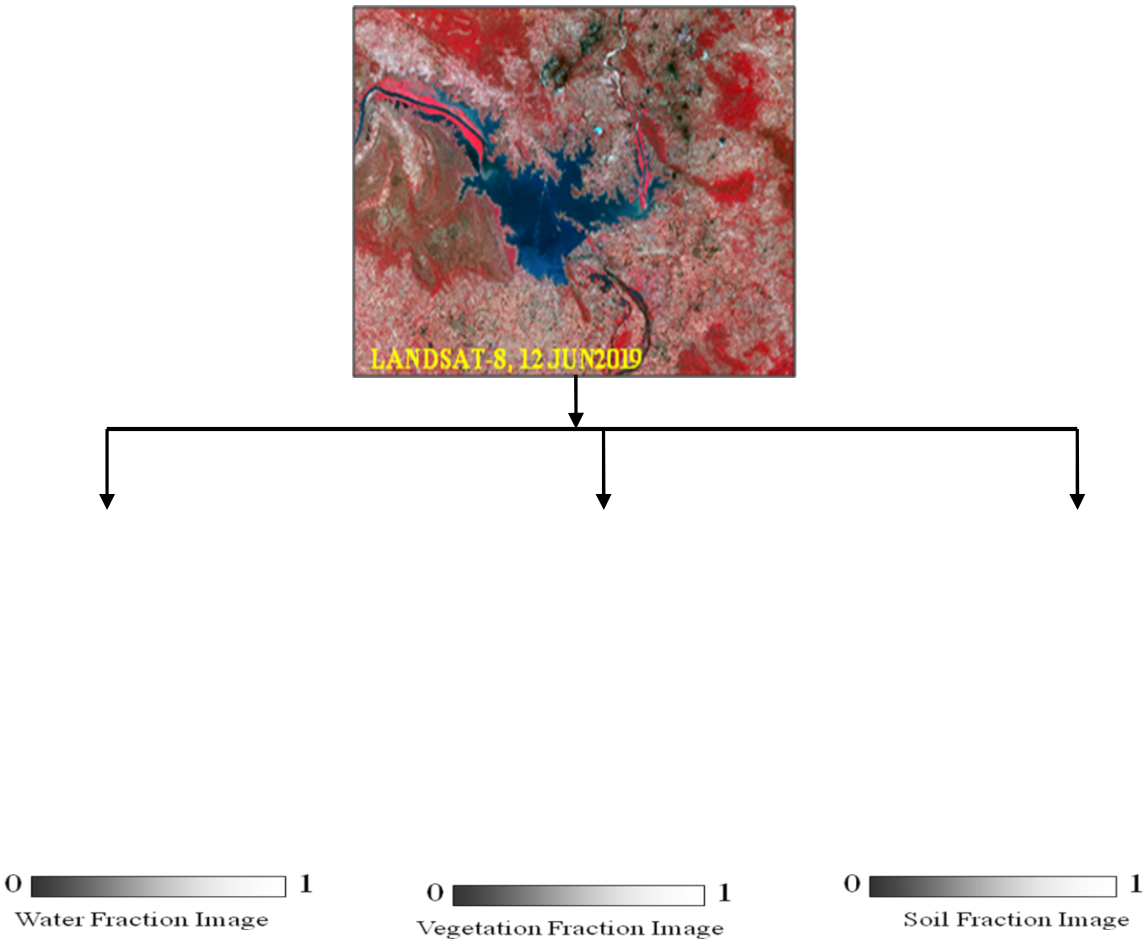

Fig.5.5. Sub-pixel classified output of Hirakud Reservoir for the water level 183.51 m

Table 5.4 Satellite data derived water spread area using sub-pixel classification approach.

Sl.No.	Satellite and Sensor	Date of Pass	Reservoir Water Level (m)	Interpreted water spread area from the satellite data (Ha)
1	LANDSAT-8 / OLI	29-Sep-18	191.84	59982.34
2	Sentinel-2A / MSI	23-Oct-18	191.38	57559.91
3	Sentinel-2A / MSI	22-Nov-18	190.82	54706.93
4	Sentinel-2A / MSI	31-Jan-19	189.78	49688.44
5	Sentinel-2A / MSI	20-Feb-19	189.20	47047.70
6	LANDSAT-8 / OLI	25-Apr-19	186.75	37141.46
7	LANDSAT-8 / OLI	11-May-19	185.48	32801.02
8	LANDSAT-8 / OLI	27-May-19	184.22	29030.94
9	LANDSAT-8 / OLI	12-Jun-19	183.51	27141.78

As explained earlier, a second order polynomial equation (6.2) was fitted for the water spread area arrived using sub-pixel classification approach and the revised water spread areas at regular intervals were calculated and given in Table 5.5.

Water Spread Area in hectare = $(168.197 * L^2) - (59190.3 * L) + 5224965$ (6.2)

Where L = Reservoir water level in meter

Table 5.5 Water spread area estimated at regular intervals using sub-pixel classification approach

Sl.No.	Reservoir elevation above M.S.L (m)	Water-spread area estimated using sub-pixel approach (Ha)
1.	192.02 (FRL)	60949.62 (609.49 Mm^2)
2.	191	55612.46
3.	190	50719.7
4.	189	46163.34
5.	188	41943.37
6.	187	38059.79
7.	186	34512.61
8.	185	31301.83
9.	184	28427.43
10.	183	25889.43
11.	182	23687.83
12	181	21822.62
13.	180	20293.8
14.	179.83 (MDDL)	20067.36

The revised water-spread areas that were estimated using sub-pixel classification approach at regular intervals were utilized to compute the volumes between the MDDL and FRL. The volumes thus calculated have been added up to find out the cumulative live storage capacity of the reservoir. The estimated cumulative live storage capacity of the Hirakud reservoir, according to the sub-pixel classification approach, for the period 2018-19 was **4431.91 M.cum**. The difference between the 1956 live capacity and the present live capacity reveals the amount of sediment deposited during 63 years of operation of the reservoir, which is estimated at **1410.96 M.cum**. Therefore, from the sub-pixel approach calculations, it is assessed that 1410.96 M.Cum of sediment has been deposited in the Hirakud reservoir during the period 1957 to 2019. Hence, the rate of sedimentation in the live storage capacity of Hirakud reservoir is estimated at 22.39 M.Cum/year. The calculations are given in Table 5.6.

Table 5.6 Reservoir capacity estimation using Sub-pixel classification approach

Sl.No.	Reservoir elevation above M.S.L (m)	Water-spread area estimated using sub-pixel approach (Ha)	Cumulative Capacity (Ha-m)
1.	192.02 (FRL)	60949.62 (609.49 Mm^2)	443191.5 (4431.91 Mm^3)
2.	191	55612.46	383769.5
3.	190	50719.7	330622.2
4.	189	46163.34	282203.5
5.	188	41943.37	238167
6.	187	38059.79	198181.1
7.	186	34512.61	161909.4
8.	185	31301.83	129015.2
9.	184	28427.43	99162.14
10.	183	25889.43	72013.59
11.	182	23687.83	47233.11
12	181	21822.62	24484.26
13.	180	20293.8	3430.68
14.	179.83 (MDDL)	20067.36	0

5.3 Estimation of rate of sedimentation using super-resolution modeling approach.

In this study super resolution technique using Hopfield Neural Network which enhances the resolution of output images was applied. From the multi-spectral satellite image at 30 m spatial resolution, a set of proportion images for each land cover class was obtained by the linear spectral unmixing. The super resolved maps of the multispectral images were obtained from the water fraction image by incorporating the Hopfield Neural Network algorithm. A single pixel of water fraction image which has a resolution of 30 m (LANDSAT-8/OLI) was sub-divided and enhanced to super resolved map wherein every element has pixel size of 6 m. Each pixel of the sub-divided fraction image is an input into the neural network and processed by a set of 5 x 5 (25) neurons. Since a zoom factor of 5 is adopted, the network for each pixel processing is constructed with 25 neurons. In the case of Sentinel-2 data which have spatial resolution of 10 m, a zoom factor of 2 is adopted, hence the super resolved map, have a pixel size of 5 m. If a super resolved pixel has an area

proportion for a particular landcover class as 100%, all neurons are given a value of 0.55. Similarly, if a pixel has an area proportion for particular landcover class as 50%, 13 neurons are given a value of 0.55 and 12 neurons are given a value of 0.45. The concept of spatial order within and outside a pixel is the basis for determining the energy of the network. The point at which minimum energy occurs is the stable state of the network. The neuron outputs at this point determine the best accurate map of the given image. Thus, prediction of the spatial pattern of the water bearing pixels is made accurately at the super resolution scale and finally the exact boundary of reservoir is obtained. The output of super resolved map contains values only 0 and 1. The value 0 and 1 implies non-water and water pixels respectively. First, the pixels which have value of 1 were separated out from the super resolved map. Then, the number of pixels which have value of 1 was multiplied by the size of the super resolved map size i.e 6 m x 6 m or 5 m x 5 m as the case may be. Thus, the water spread area occupied by a particular water level has been obtained. Here it is worth mentioning that the super resolved map produces higher resolution map than the input one, hence the accuracy of classification increases. Therefore, the accuracy of water-spread area estimated using super resolved map would have more accurate results than the per-pixel and sub-pixel classified approaches. The water spread area estimated using super resolution mapping is given in Table 5.7.

Table 5.7 Satellite data derived water spread area using super-resolution approach.

Sl.No.	Satellite and Sensor	Date of Pass	Reservoir Water Level (m)	Interpreted water spread area from the satellite data (Ha)
1	LANDSAT-8 / OLI	29-Sep-18	191.84	60139.64
2	Sentinel-2A / MSI	23-Oct-18	191.38	57717.21
3	Sentinel-2A / MSI	22-Nov-18	190.82	54864.23
4	Sentinel-2A / MSI	31-Jan-19	189.78	49845.74
5	Sentinel-2A / MSI	20-Feb-19	189.20	47205.00
6	LANDSAT-8 / OLI	25-Apr-19	186.75	37298.76
7	LANDSAT-8 / OLI	11-May-19	185.48	32958.32
8	LANDSAT-8 / OLI	27-May-19	184.22	29188.24
9	LANDSAT-8 / OLI	12-Jun-19	183.51	27299.08

In order to estimate the water spread area at regular water intervals and for the missing water levels, a second order polynomial equation (6.3) was fitted and the revised water spread areas were calculated. The water spread areas at regular intervals are given in Table 5.8.

$$\text{Water Spread Area in hectare} = (168.197 * L^2) - (59190.3 * L) + 5225122 \quad (6.3)$$

Where L = Reservoir water level in meter

Table 5.8 Water spread area estimated at regular intervals using super-resolution approach.

Sl.No.	Reservoir elevation above M.S.L (m)	Water-spread area estimated using super-resolution approach (Ha)
1.	192.02 (FRL)	61106.62
2.	191	55769.46
3.	190	50876.7
4.	189	46320.34
5.	188	42100.37
6.	187	38216.79
7.	186	34669.61
8.	185	31458.83
9.	184	28584.43
10.	183	26046.43
11.	182	23844.83
12	181	21979.62
13.	180	20450.8
14.	179.83 (MDDL)	20224.36

The revised water-spread areas were utilized to compute the volumes between the MDDL and FRL. The volumes thus calculated have been added up to find out the cumulative live storage capacity of the reservoir. The estimated cumulative live storage capacity of the Hirakud reservoir, according to the per-pixel classification approach, for the period 2018-19 was 4451.06 M.cum. The difference between the 1956 live capacity and the present live capacity reveals the amount of sediment deposited during 63 years of operation of the reservoir, which is estimated at 1391.62 M.cum. Therefore, from the per-pixel approach calculations it is assessed that 1391.82 M.Cum of sediment has been deposited in the Hirakud reservoir during the period 1957 to 2019. Hence, the rate of sedimentation in the live storage capacity of Hirakud reservoir is estimated at 22.09 M.Cum/year. The live storage capacity calculations are given in Table 5.9.

Table 5.9 Hirakud Reservoir's live storage capacity estimation using super resolution mapping approach

Sl.No.	Reservoir elevation above M.S.L (m)	Water-spread area estimated using super resolution approach (Ha)	Cumulative Capacity (Ha-m)
1.	192.02 (FRL)	61106.62 (611.06 Mm^2)	445106 (4451.06 Mm^3)
2.	191	55769.46	385523.8
3.	190	50876.7	332219.4
4.	189	46320.34	283643.7
5.	188	42100.37	239450.1
6.	187	38216.79	199307.2
7.	186	34669.61	162878.4
8.	185	31458.83	129827.2
9.	184	28584.43	99817.01
10.	183	26046.43	72511.41
11.	182	23844.83	47573.88
12	181	21979.62	24667.99
13.	180	20450.8	3457.37
14.	179.83 (MDDL)	20224.36	0

5.4 Validation of per-pixel, sub-pixel and super-resolution approaches

Several researchers (Esimann and Hardie 2005, Lamyaa and Salwa 2010, Haerttel et al. 2004, Foody 2007) have shown that the information obtained from per-pixel, sub-pixel and super resolution can be compared to the satellite data that has been obtained at higher resolution. In line with the above findings, it was decided to validate the water spread obtained by per-pixel, sub-pixel and super resolution classification approaches with the water spread of high resolution image data which have a spatial resolution of 5m (Resourcersat-2A-LISS-IV-Mx). However, concurrent high resolution data was not available for all the nine images used in the study. Therefore, the validation was carried out with the only available two image data for the water level 191.84m and 189.20m. The results of experiments carried out on the validation set are given in the Table 5.10. The Table 5.11 reveals that the super resolution approach produced very less error (4.44%) than the per-pixel (5.39%) and sub-pixel (5.02%) based approaches. This shows that the super resolution based approach can be applied to estimate the capacity of the reservoirs with higher accuracy than the per-pixel and sub-pixel based approaches.

Table 5.10 Validation of per-pixel, sub-pixel and super-resolution approaches.

Satellite/Sensor Date of Satellite Pass		Reservoir Elevation above m.s.l (m)	Water-spread area Per-Pixel (Mm^2)	Water-spread area Sub-Pixel (Mm^2)	Water-spread area Super-Resolution (Mm^2)	Res-2A-LISSIV (Mx) Water-spread area (5m) (Mm^2)
20 Sep 2018 (Validation-1)	Landsat-8 30m	191.84	598.81	599.82	601.39	620.86
20 Feb 2019 (Validation2)	Sentinel-2A 10 m	189.20	469.47	470.48	472.05	478.27

Table 5.11 Percentage (%) of error between per-pixel, sub-pixel and super-resolution based approaches.

No. of Validation	Processing Approach		
	Per-pixel	Sub-pixel	SRM
Validation-1	3.55%	3.39%	3.14
Validation-2	1.84%	1.63%	1.30
Vali1 + Vali2	**5.39%**	**5.02%**	**4.44%**
Average Error	**2.70%**	**2.51%**	**2.22%**

5.5 Comparison of Elevation- area- capacity of Hirakud reservoir with original and other surveys.

The results obtained by best capacity estimation (SRM approach) have been compared with original, hydrographic surveys and Rule Curve Revisions. The comparison is shown in Table No.12. The comparison reveals that Hirakud reservoir water spread area and the volume at all the water levels is gradually reducing. The water spread area at the lowest level shows slight increase. The reason for this is the satellite observation was to the lowest water level 183.51m, which is 3.68 m above MDDL. From 183.51 to 179.83 the estimation was arrived through regression analysis. The siltation rate obtained by super-resolution based survey closely agrees with the earlier surveys (Table 5.13) carried out. The comparison between Original (1956), Rule Curve Revision (2000) and the SRM approach (2019) capacity curve is given in Figure 5.6.

Table 5.12 Elevation- area- capacity of Hirakud as per original (1956), 1986, 1995, 2019 surveys and 1988 and 2000 rule curve revisions

Elevation in feet	Elevation in m	Original 1956		3rd cycle hydrographic survey 1986		Rule Curve Revision Committee 1988		Remote sensing survey by CWC 1995		Revised ending 2000		SRM based Remote sensing survey, 2019	
		Area (ha)	Live storage (ha-m)	Area (ha)	Live storage (ha-m)	Area (ha)	Live storage (ha-m)	Area (ha)	Live storage (ha-m)	Area (ha)	Live storage (ha-m)	Area (ha)	Live storage (ha-m)
630	192.02	72735	584288	61930	510605	61214	537817	69115	490152	69507	482361	61107	445107
625	190.50	65494	479699	56771	421230	56114	451100	60815	391209	59900	385212	53281	358211
620	188.98	58253	376792	51590	339645	50994	365000	53020	304531	52586	300753	46233	282672
615	187.45	52451	300681	47706	264875	47154	280504	45729	229349	44562	227858	39923	216851
610	185.93	46648	228271	43333	196331	42832	201928	38942	164894	37222	166504	34434	160424
605	184.40	41651	157679	38666	134603	38219	138772	32660	110397	32099	114476	29694	111451
600	182.88	36654	90787	33515	80283	33128	85113	26882	65089	27347	69868	25764	69381
595	181.36	32211	45394	25197	36214	24906	40706	21609	28203	23231	31916	22612	32694
590	179.83	27767	0	22896	0	22631	0	17022	0	19316	0	20224	0

Table 5.13 Sedimentation rate for live storage for 1957- 1986, 1957- 1995 and 1957- 2019

Sedimentation rate	1957-1986	1957-1995	1957-2019
Reduction in Live Storage (Ha m)	72000 (720 Mm^3)	92453 (924.53Mm^3)	139182.47 (1391.82 Mm^3)
Reduction in Live Storage (Ha m/ year)	2400 (24.0 Mm^3/y)	2371 (23.71 Mm^3/y)	2209.24 (22.09 Mm^3/y)
Reduction in Live Storage (%)	12.36%	15.87%	23.82%
Reduction in Live Storage / year (%)	0.412%	0.407%	0.38%
Reduction in Live Storage (Ha m/100 sq.km/year)	2.878	2.842	2.70

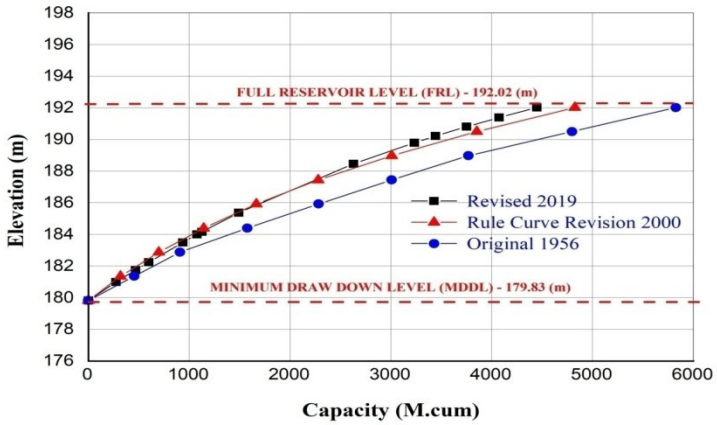

Fig. 5.6. Comparison of Original (1956), Rule Curve Revision (2000) and SRM approach (2019) capacity curve.

Part-II : Assessment of sedimentation using microwave satellite data:

5.6 Estimation of rate of sedimentation by microwave satellite data

The pre-processing steps which are mandatory for any microwave data analysis and to get the required information are explained in the methodology section. These procedures have been carried out for all the eleven Sentinel-1A data used in this study using SNAP platform.

The bimodal histogram distribution of the SAR image (Fig.5.7) reveals that the lower peak represents the pixels corresponding to specular reflection. The pixels from the specular reflection mostly pertain to water pixels. The average sigma nought (σ0) value of water pixels in this study ranges from -40.62db to -21.58db (db pronounced as decibel). The higher peak represents pixels with diffuse reflection (land features) in the study area. The value of land pixels ranges from -20db to 5db. The pixels pertaining to reservoir water spread area has been separated out from the land area for further processing. The full image and the separated water spread area pertaining to the near FRL (190.19m) which is on 10th October 2018 is shown in the Fig 5.7.

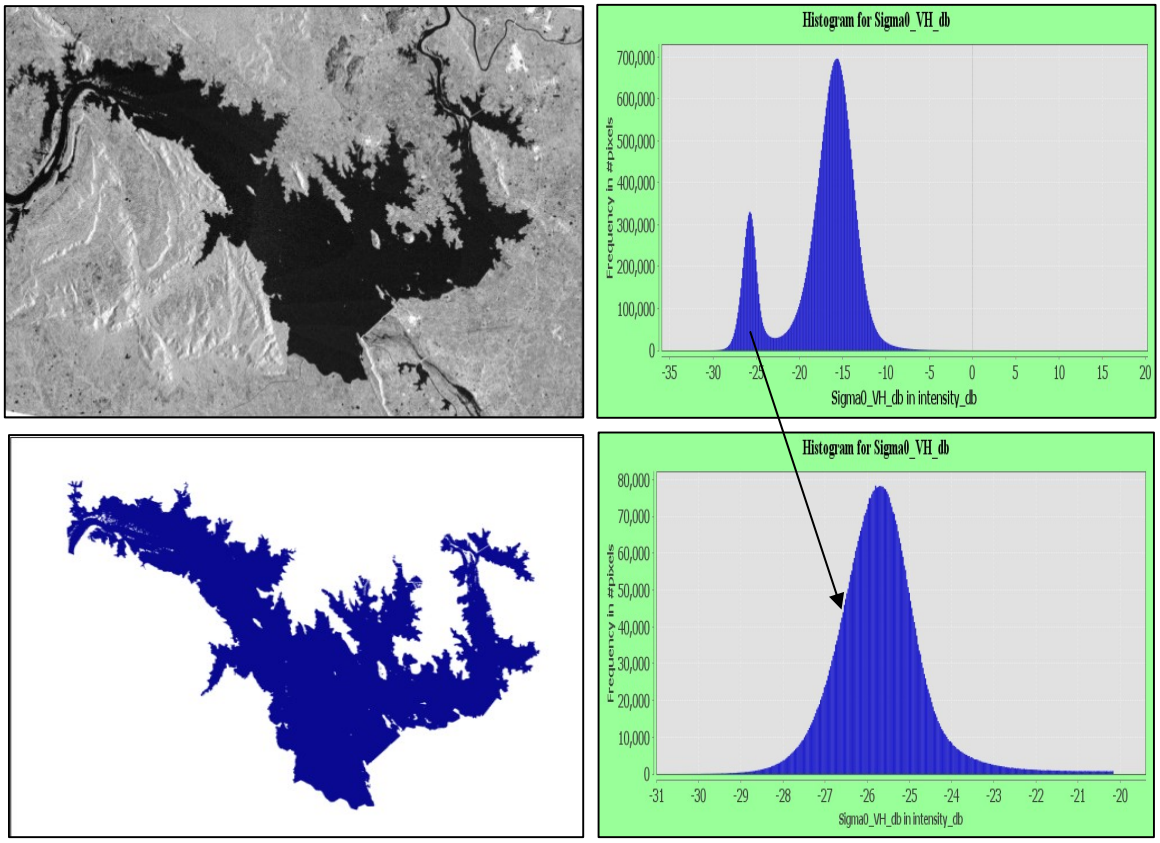

Figure 5.7 Histogram of SAR image & extracted water spread area pertaining to 10-oct-2018.

The water features in the SAR imagery are the result of different factors such as acquisition characteristics (wavelength, incident angle, and polarization), soil moisture, and soil surface conditions. In SAR image the water pixels have low backscatter as compared to other landscapes due to specular reflection. Therefore, the water pixels appear darker in color with respect to other features of the image, which makes the water pixels to be recognized easily. The previous studies shows that dual-polarization data provides the most informative

result and the thresholding is viewed an efficient class extraction method form the stable water. Therefore, in this study the water pixels were extracted using VV or VH polarized data through thresholding class extraction methodology. The threshold values were identified by analyzing the image histogram and interacting with the imagery. The identified threshold values and the extracted water spread area from the respective VV or VH bands are given in the Table 5.14 and Fig 5.8. With the help of identified threshold values, water pixels were recognized and their water spread areas were estimated.

Table 5.14. Microwave image data (Sentinel-1A) derived water spread area

Sl.No.	Date of Image acquisition	Reservoir Water Level (m)	Threshold limits (dB)	Water-spread area estimated using Sentinel-1A data (Ha)
1	10-Oct-2018	190.19	-34.73 to -19.24	51614.14
2	27-Nov-2018	189.23	-34.54 to -20.16	47172.21
3	26-Jan-2019	188.42	-32.48 to -20.12	43665.48
4	03-Mar-2019	187.41	-37.80 to -21.58	39602.07
5	27-Mar-2019	186.66	-36.18 to -19.20	36806.71
6	08-Apr-2019	186.17	-36.80 to -19.54	35082.60
7	20-Apr-2019	185.55	-35.54 to -19.58	33016.83
8	2-May-2019	184.80	-40.62 to -19.70	30690.73
9	14-May-2019	183.81	-40.51to -19.34	27910.03
10	26-May-2019	182.86	-33.61 to -19.25	25551.66
11	19-Jun-2019	181.79	-31.18 to -14.37	23258.93

In order to estimate the water spread area at regular water intervals and for the missing water levels, a second order polynomial equation (6.4) was fitted and the revised water spread areas were calculated. The water spread areas at regular intervals are given in Table 5.15.

$$\text{Water Spread Area in hectare} = (168.197 * L^2) - (59190.3 * L) + 5224955.7 \quad (6.4)$$

Where L = Reservoir water level in meter

Based on the Sentinel-1A derived water-spread area, a regression analysis has been used to find out the revised water-spread areas and volumes between the live storage capacity of the reservoir, 179.83m (MDDL) to 192.02 (FRL). The estimated cumulative live storage capacity of the Hirakud reservoir, using microwave satellite data (Sentinel-1A) for the period 2018-19 was 4430.78 M.cum. The difference between the 1956 live capacity and the present live capacity reveals the amount of sediment deposited during 63 years of operation of the reservoir, which is estimated at 1412.09 M.cum. Therefore, using microwave data it is assessed that 1412.09 M.Cum of sediment has been deposited in the Hirakud reservoir during the period 1957 to 2019. Hence, the rate of sedimentation in the live storage capacity of Hirakud reservoir is estimated at 22.41 M.Cum/year. The calculations are given in Table 5.16.

Table 5.15 Water spread area estimated at regular intervals using super-resolution approach.

Sl.No.	Reservoir elevation above M.S.L (m)	Water-spread area estimated using Sentinel-1A data (Ha)
1.	192.02 (FRL)	60940 (609.40 Mm^2)
2.	191	55603
3.	190	50710
4.	189	46154
5.	188	41934
6.	187	38050
7.	186	34503
8.	185	31293
9.	184	28418
10.	183	25880
11.	182	23679
12	181	21813
13.	180	20285
14.	179.83 (MDDL)	20058

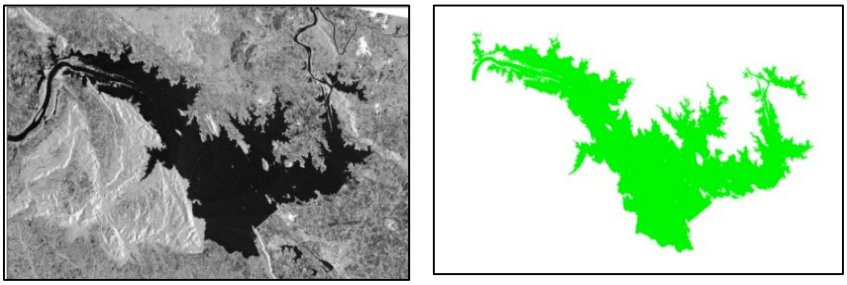

27-Nov-2018, Water Level – 189.23 m

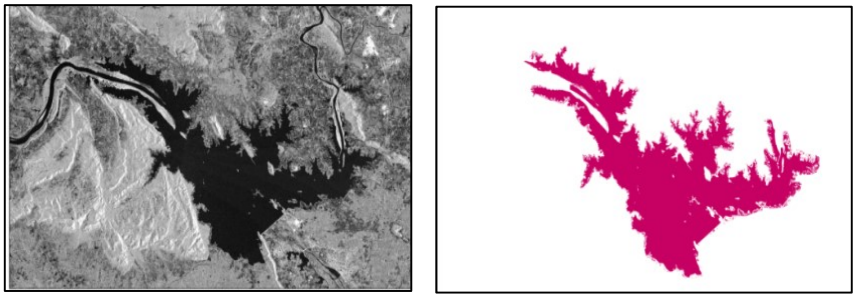

02-May-2019, Water Level – 184.80 m

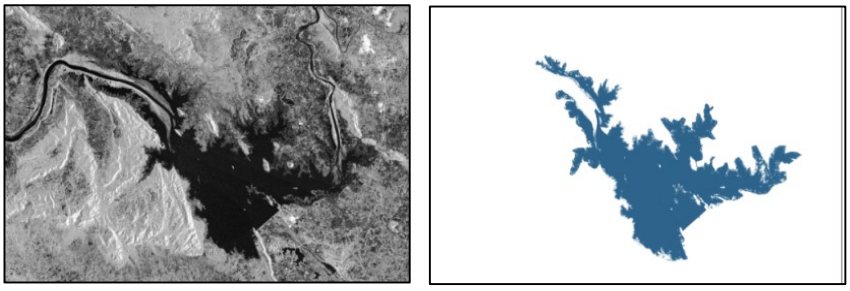

19-Jun-2019, Water Level – 181.79 m

Figure 5.8 Water spread area extracted from Sentinel-1A data of Hirakud Reservoir for three different satellite pass.

Table 5.16. Reservoir capacity estimation using microwave satellite data (Sentinel-1A).

Sl.No.	Reservoir elevation above M.S.L (m)	Water-spread area estimated using per-pixel approach (Ha)	Cumulative Capacity (Ha-m)
1.	192.02 (FRL)	60940 (609.40 Mm^2)	443078 (4430.78 Mm^3)
2.	191	55603	383666
3.	190	50710	330528
4.	189	46154	282118
5.	188	41934	238091
6.	187	38050	198114
7.	186	34503	161852
8.	185	31293	128967
9.	184	28418	99123
10.	183	25880	71984
11.	182	23679	47213
12	181	21813	24473
13.	180	20285	3429.1
14.	179.83 (MDDL)	20058	0

CHAPTER-6

CONCLUSIONS AND SCOPE OF FUTURE WORK

Water spread area and capacity of reservoirs is important parameters for the reservoir management authorities. The ever changing environment scenarios affect the amount of sediment deposited in to a reservoir. Three different optical methodologies have been employed to identify the best methodology, so that the capacity and amount of siltation in the reservoir can be precisely estimated. Apart from this the microwave satellite data has also been utilized to find out its feasibility to assess the capacity of Hirakud reservoir.

In the per-pixel classification approach band threshold technique was utilized to extract the water pixels from the satellite images. This algorithm needs separate minimum and maximum threshold DN values from the NIR band. With the help of the said algorithm, the pixels which contain the DN numbers between the identified minimum and maximum threshold values were labeled as water pixels. The total number of water pixels that were extracted was multiplied by the area of a single-pixel to compute the water spread area (WSA) occupied by a particular water level. This technique was adopted to convert the extracted water pixels into the water spread area in all the nine images used in this study. From the per-pixel derived WSA the live storage capacity of the reservoir was estimated and the rate of sedimentation is arrived at 22.56 M.Cum/year.

.

The sub-pixel approach has been adopted and applied to all the nine images of the reservoir. After, selecting appropriate end-members, the SPC resulted in fraction images which contain sub-pixel level information about the reservoir and its peripheral region. Information derived from the water fraction image, has been translated in to water-spread area and the capacity of the reservoir was calculated. SPC derived rate of sedimentation is 22.39 M.Cum/year.

The super resolved maps of the multispectral images were obtained from the water fraction image by incorporating the Hopfield Neural Network algorithm. The concept of spatial order within and outside a pixel is the basis for determining the energy of the network. The point at which minimum energy occurs is the stable state of the network. The neuron output at this point determines the best accurate map of the given image. Thus, prediction of the spatial pattern of the water bearing pixels is made accurately at the super resolution scale and finally the exact boundary of reservoir is obtained. The super resolved map produces higher resolution map than the input one, hence the accuracy of classification increases. The output of super resolved map contains values only 0 and 1. The value 0 and 1 implies non-water and water pixels respectively. The pixels which have value of 1 were separated out from the super resolved map and the water spread area pertaining to all the nine images were estimated. From the SRM derived WSA the live storage capacity of the reservoir was estimated and the rate of sedimentation is arrived at 22.09 M.Cum/year.

The Odisha region is often affected by cyclonic storms and severe monsoon activities, in such situations optical data cannot be used and therefore usage of microwave data will provide continuous satellite data for the delineation of reservoir water-spread area. The water spread area from the Sentinel-1A, SAR data have been delineated after following the mandatory pre-processing procedures. The average sigma nought ($\sigma 0$) value of water pixels in this study ranges from -40.62db to -21.58db. Water pixels were extracted using VV or VH polarized data through thresholding extraction method. The analysis reveals that the rate of

sedimentation in the live storage capacity of the reservoir using microwave data is 22.41 M.Cum/year.

The water spread area from the satellite data is the only input used in the per-pixel, sub-pixel and super resolution approaches for the estimation of capacity of the reservoir and the rate of sedimentation. The capacity has been calculated using 30m and 10m resolution data. The prior studies shows that the information obtained from per-pixel, sub-pixel and super resolution can be compared to satellite data that has been obtained at higher resolution. In line with this the water spread area obtained by per-pixel, sub-pixel and super resolution classification approaches have been validated with the water spread area of high resolution image data which have a spatial resolution of 5m (Resourcersat-2A-LISS-IV-Mx). The validation reveals that the super resolution approach produced very less error (4.44%) than the per-pixel (5.39%) and sub-pixel (5.02%) based approaches. This shows that the super resolution based approach can be applied to estimate the capacity of the reservoirs with higher accuracy than the per-pixel and sub-pixel based approaches.

Amount of annual incoming sediment in to the reservoir is assessed, this implies that soil conservation measures has to be adopted in the catchment area. There are many mathematical models which estimate, watershed wise sediment yield, with the help of these models the most vulnerable watershed Hirakud catchment can be identified and appropriate soil conservation measures would further reduce siltation in the Hirakud reservoir.

REFERENCES

1. Amitrano, D., di Martino, G., Iodice, A., Mitidieri, F., Papa, M. N., Riccio, D., & Ruello, G. (2014). Sentinel-1 for monitoring reservoirs: A performance analysis. *Remote Sensing*, *6*(11), 10676–10693. https://doi.org/10.3390/rs61110676

2. Aplin, P. and Atkinson, P.M. "Sub-pixel land cover mapping for per-field classification", International Journal of Remote Sensing, Vol. 22 No. 14, pp. 2853-2858, 2001.

3. Arora, M. K., and Foody, G. M. "Log-linear Modelling for the Evaluation of Variables Affecting the Accuracy of Probabilistic, Fuzzy and Neural Network Classifications", International Journal of Remote Sensing, Vol.18, No.4, pp.785-798, 1997.

4. Atkinson, P.M. "Mapping sub-pixel proportional land cover with AVHRR imagery", International Journal of Remote Sensing, Vol. 18, No. 4, pp. 917-935, 1997.

5. Bajjouk, T., Populus, J. and Guillaumont, B. "Quantification of sub- pixel cover fractions using PCA and a linear programming method", Application to the Coastal Zone of Riscoff (France). Remote Sensing of Environment, Vol. 64, pp. 153-165, 1998.

6. Bateson, A. and Curtiss, B. "A method for manual endmember selection and spectral unmixing", Remote Sensing of Environment, Vol. 55, pp.229-243, 1996.

7. Bazi, Y., Bruzzone, L., & Melgani, F. (2007). Image thresholding based on the EM algorithm and the generalized Gaussian distribution. *Pattern Recognition*, *40*(2), 619–634. https://doi.org/10.1016/j.patcog.2006.05.006.

8. Boardman, J. "Inversion of high spectral resolution data", SPIE Symposium, Vol. 12, pp. 222-233, 1990.

9. Boardman, J.W. "Automating spectral unmixing of AVIRIS data using convex geometry concepts", Summaries of the Fourth annual JPL Airborne Geoscience Workshop, (California: JPL), pp.11-14, 1993.

10. Boardman, J.W., and Kruse, F.A. "Automated spectral analysis: A geologic example using AVIRIS data", North Grapevine Mountains, Nevada, Proceedings of Tenth Thematic Conference on Geologic Remote Sensing, San Antonio, TX, pp. 407-418, 1994.

11. Boardman, J. W., Kruse, F. A., and Green, R. O. "Mapping target signatures via partial unmixing of AVIRIS data", Fifth JPL Airborne Earth Science Workshop, Pasadena (California: JPL), Vol. 95-1, pp. 23-26, 1995.

12. Bolanos, S., Stiff, D., Brisco, B., & Pietroniro, A. (2016). Operational surface water detection and monitoring using Radarsat 2. *Remote Sensing*, *8*(4). https://doi.org/10.3390/rs8040285.

13. Borel, C.C. and Gerstl, S.A.W. "Non-linear of spectral unmixing models for vegetative and soil surface", Remote Sensing of Environment, Vol. 47, No. 3, pp. 403-416, 1994.

14. Bouthayna Msellmi, Z. B. Rabah, I. R. Farah (2016). Super-resolution algorithm based on sub-pixels spatial Correlation for hyperspectral image classification. 2nd International Conference on Advanced Technologies for Signal and Image Processing.

15. Bosdogianni, P., Petrou, M. and Kittler, J. "Mixed pixel classification with robust statistics", IEEE Transactions on Geoscience and Remote Sensing, Vol. 35, No. 3, pp. 551-559, 1997.

16. Bryant Emily, S., Pangburn Timothy, Bolus L, R, Pedrick, A.G., Peacock, Gregory., Tracy, G.B. and Evelyn, B.J. "Painted Rock Reservoir-1993 Water Surface Area and Storage Capacity Estimate Derived from Landsat Data Classification", Special report (99-6) by U.S. Army Corps of Engineers, Los Angeles, California, 1999.

17. Bryant, R.G. "Validated linear mixture modelling of Landsat TM data for mapping evaporate minerals on a playa surface", methods and applications, International Journal of Remote Sensing, Vol. 17, No. 2, pp. 315-330, 1994.

18. Carola Gómez-Rodríguez, Javier Bustamant and Carmen Díaz-Paniagua, "Evidence of Hydro-period Shortening in a Preserved System of Temporary Ponds", Remote Sensing Letters, Vol. 2, pp.1439-1462, 2010.

19. Casals-Carrasco P., Kubo, S. and Babu Madavan B. "Application of spectral mixture analysis for terrain evaluation studies", International Journal of Remote Sensing,Vol.21, No.16, pp. 3039-3055, 2000.

20. Chauhan, S., & Srivastava, H/. S. (2016). Comparative Evaluation of the Sensitivity of Multi-Polarised Sar and Optical Data for Various Land Cover. *International Journal of Advancement in Remote Sensing, GIS and Geography COMPARATIVE*, *4*(1), 1–14.

21. Chen, Y., Qiao, S., Zhang, G., Xu, Y. J., Chen, L., & Wu, L. (2020). Investigating the potential use of Sentinel-1 data for monitoring wetland water level changes in China's Momoge National Nature Reserve. *PeerJ*, *8*, e8616.

22. CWC. Compendium of silting of reservoirs in India, Technical report on silting of reservoirs in India, WP&P wing, Central Water Commission, New Delhi, 2001.

23. de Asis, M. Alejandro, and Omasa Kenji, “Estimation of vegetation parameter for modeling soil erosion using linear Spectral Mixture Analysis of Landsat ETM data”, Journal of Photogrammetry and Remote Sensing, Vol. 62, No. 4, pp.309-324, 2007.

24. Dennison, P. E., and Roberts, D.A. “Endmember selection for multiple endmember spectral mixture analysis using endmember average RMSE”, Remote Sensing of Environment, Vol. 87, pp.123-135, 2003.

25. Duy, N. B. (2015). Automatic detection of surface water bodies from Sentinel-1 SAR images using Valley-Emphasis method. *Vietnam Journal of Earth Sciences*, *37*(4), 328–343.

26. ERDAS Field Guide, 1999.

27. Federico Filipponi Istituto. (2019). Sentinel-1 GRD Preprocessing Workflow †. *3rd International Electronic Conference on Remote Sensing)*, *18*(1), 1–4. https://doi.org/10.3390/ECRS-3-06201.

28. Foody, G.M. “Approaches for the production and evaluation of fuzzy land cover classifications from remotely sensed data”, International Journal of Remote Sensing, Vol. 17, No. 7, pp. 1317-1340, 1994.

29. Foody, G.M. “Variability in soft classification prediction and its implications for sub-pixel scale change detection and super resolution mapping”, Photogrammetric Engineering and Remote Sensing, Vol. 73, pp. 923-933, 2007.

30. Foody, G. M., and Arora, M. K. “Incorporating Mixed Pixels in the Training, Allocation and Testing Stages of Supervised Classifications”, Pattern Recognition letters, Vol.17, Is.13, pp. 1389-1398, 1996.

31. Full, W. E, Ehrlich, R., and Bezdek, J. C. “Fuzzy Q model – a new model approach for linear unmixing”, Mathematical Geology, Vol. 14, No. 3, pp. 259-270, 1982.

32. Foody, G. M., Muslim, A. M., & Atkinson, P. M. (2005). Super resolution mapping of the waterline from remotely sensed data. International Journal of Remote Sensing, 26(24), 5381–5392.

33. Garkusha, I. N., Hnatushenko, V. V., & Vasyliev, V. V. (2017). Research of influence of atmosphere and humidity on the data of radar imaging by Sentinel-1. *2017 IEEE 37th International Conference on Electronics and Nanotechnology, ELNANO 2017 - Proceedings*, 405–408. https://doi.org/10.1109/ELNAN/O.2017.7939787.

34. Goel, M.K., Jain, S.K. and Agarwal, P.K. "Assessment of sediment deposition rate in Bargi Reservoir using digital image processing", Journal of Hydrological Sciences, Vol. 47(S), pp. S81–S92, 2002.

35. Gong, P. "Integrated analysis of spatial data from multiple sources: using evidential reasoning and artificial neural network techniques for geological mapping", Photogrammetric Engineering and Remote Sensing, Vol.62, pp. 513-523, 1996.

36. Gstaiger, V., Huth, J., Gebhardt, S., Wehrmann, T., & Kuenzer, C. (2012). Multi-sensoral and automated derivation of inundated areas using TerraSAR-X and ENVISAT ASAR data. *International Journal of Remote Sensing*, *33*(22), 7291–7304. https://doi.org/10.1080/01431161.2012.700421.

37. Heltin, G. C., & Vani, K. (2010). Super resolution mapping of satellite images using Hopfield neural networks. In IEEE Conference on RSTSCC (pp. 114–118).

38. Holland, J., & Aplin, P. (2013). Super-resolution image analysis as a means of monitoring bracken (Pteridium aquilinum) distributions. ISPRS Journal of Photogrammetry and Remote Sensing, 75, 48–63.

39. Jain, S.K., Singh, P. and Seth, S.M. "Assessment of sedimentation in Bhakra Reservoir in the western Himalayan region using remotely sensed data", Hydrological Sciences Journal, Vol. 47, No. 2, pp. 203-212, 2002.

40. Jain, S.K., Pushpendra, K.A., and Vijay, P.S. "Hydrology and water resources of India, Springer", The Netherlands, 2007.

41. Jeyakanthan, V.S., Rao, Y.R.S. and Ramasastri, K.S. "Reservoir capacity estimation using satellite data", IAPRS and SIS, Resources and Environmental Monitoring, Hyderabad, India, Vol. 34, No. 7, 2002.

42. Jeyaseelan, A.T. and Thiruvengadachari, S. "Sedimentation survey of Kuttiyadi Hydel reservoir through remote sensing method", In: Proceedings of the workshop on remote sensing and GIS application in water resources and engineering, 17–19 September 1997, Bangalore, India. India: CBIP, pp. 8–15, 1997.

43. Lee, J.S.; Jurkevich, L., Dewaele, P., Wambacq, P., Oosterlinck, A. Speckle filtering of synthetic aperture radar images: A review. *Remote Sens. Rev.* **1994**, *8*, 313-340.

44. Lobell, B.D., and Asner, P.G., "Cropland distributions from temporal un-mixing of MODIS data", Remote Sensing of Environment, Vol. 93, pp. 412-422, 2004.

45. Liu, C. (2016). Analysis of Sentinel-1 SAR data for mapping standing water in the Twente region. *University of Twente - ITC*. http://www.itc.nl/library/papers_2016/msc/wrem/cliu.pdf.

46. Liu, M., Dai, Y., Zhang, J., Zhang, X., Meng, J., & Xie, Q. (2015). PCA-based sea-ice image fusion of optical data by HIS transform and SAR data by wavelet transform. *Acta Oceanologica Sinica*, *34*(3), 59–67.

47. Lu Dengsheng, Emilio Morana, and Mateus Batistellab, "Linear mixture model applied to Amazonian vegetation classification", Remote Sensing of Environment, Vol. 85, pp. 456-469, 2003.

48. Magome, J., Takeuchi, K. and Ishidaira, H. "Estimating water storage in reservoirs by satellite observations and digital elevation model: A case study of the Yagisawa Reservoir", Journal of Hydroscience and Hydrulic Engineering, Vol. 20, No. 1, pp. 49-57, 2002.

49. Manavalan, P., Sathyanath, P. and Rajegowda, G.L. "Digital image analysis technique to estimate water-spread for capacity evaluations of reservoirs", PE and RS, Vol. 59, No. 9, pp. 1389-1395, 1993.

50. Manavalan, P., Sathyanath, P., Sathyanarayn, M. and Raje Gowda, G.L. "Capacity evaluation of the Malaprabha reservoir using digital analysis of satellite data", Tech. Report no. RC: BO: WR: 001:90, Regional Remote Sensing Service Centre, Bangalore and Karnataka Engineering Research Station, Krishnarajsagar, India, 1990.

51. Marzano, F. S., Mori, S., Chini, M., Pulvirenti, L., Pierdicca, N., Montopoli, M., & Weinman, J. A. (2011). Potential of high-resolution detection and retrieval of precipitation fields from X-ban/d spaceborne synthetic aperture radar over land. *Hydrology and Earth System Sciences*, *15*(3), 859–875. https://doi.org/10.5194/hess-15-859-2011.

52. Mertens C Koen., Bernard de Baets, Verbeke, P.C. Lieven and Robert R. de Wulf. "A sub-pixel mapping algorithm based on sub-pixel/pixel spatial attraction models", International Journal of Remote Sensing Vol.27, No.15, pp. 3293-3310, 2006.

53. Milton, E.J. Image endmembers and the scene model, Canadian Journal of Remote Sensing, Vol. 25, pp.114-120, 1999.

54. Mohanty, R. B., Mahapatra, G., Mishra, D., and Mahapatra, S. S. Report on application of remote sensing to sedimentation studies in Hirakud reservoir. Orissa Remote Sensing Application Centre, Bhubaneswar and Hirakud Research Station, Hirakud, India, 1986.

55. Muad, A. M., & Foody, G. M. (2012). Super-resolution mapping o lakes from imagery with a coarse spatial and fine temporal resolution. International Journal of Applied Earth Observation and Geoinformation, 15, 79–91.

56. Nagler, T., Rott, H., Ripper, E., Bippus, G., & Hetzenecker, M. (2016). Advancements for snowmelt monitoring by means of Sentinel-1 SAR. *Remote Sensing*, *8*(4), 348.

57. Nguyen, M. Q., Atkinson, P. M., & Lewis, H. G. (2006). Super resolution mapping using a Hopfield neural network with fused images. IEEE Transactions on Geoscience and Remote Sensing, 44(3), 736–749.

58. Paintera, H. Thomas, Jeff Dozierb, Dar A. Robertsc, Robert E. Davisd, Robert O. Greene. "Retrieval of subpixel snow-covered area and grain size from imaging spectrometer data", Remote Sensing of Environment, Vol. 85, pp. 64-77, 2003.

59. Pankaj,M. and Chakravorty, B. "Remote sensing based sedimentation study in Maithon reservoir", Journal of Indian Society of Remote Sensing, Vol.35, No.1, pp. 117–120, 2007.

60. Park, J.W., Korosov, A., Babiker, M. Efficient thermal noise removal of Sentinel-1 image and its impacts on sea ice applications. In the Proceedings of the EGU General Assembly Conference Abstracts, Vienna, Austria, 23–28 April 2017; Volume 19, p. 12613.

61. Peddle, D.R. and Smith, A.M. "Spectral mixture analysis of agricultural crops: End-member validation and biophysical estimation in potato plots", International Journal of Remote Sensing, Vol. 26, No. 22, pp.4959-4979, 2005.

62. Peng, D. Z., Xiong, L. H., Guo, S. L., and Shu, N. "Study of Dongting Lake area variation and its influence on water level using MODIS data", Journal of Hydrological Sciences, Vol. 50, Is. 1, pp. 31-44. 2005.

63. Peng, Dingzhi., Guo, Shenglian., Liu, Pan. and Liu, Ting. "Reservoir Storage Curve Estimation Based on Remote Sensing Data", Journal of Hydrologic Engineering, Vol.11, No. 2, pp. 165-172, 2006.

64. O'Grady, D., Leblanc, M., & Gillieson, D. (2013). Relationship of local incidence angle with satellite radar backscatter for different surface conditions. *International Journal of Applied Earth Observation and Geoinformation*, *24*(1), 42–53. https://doi.org/10.1016/j.jag.2013.02.005.

65. Quarmby, N. A., Townsend, J.G.R., Settle, J.J., White, K. H., Milnes, M., Hindle, T. L. and Silleos, N. "Linear mixture modelling applied to A VHRR data for crop area estimation", International Journal of Remote Sensing, Vol. l3, No. 3, pp. 415-425, 1992.

66. Pham-Duc, B., Prigent, C., & Aires, F. (2017). Surface water monitoring within Cambodia and the Vietnamese /Mekong Delta over a year, with Sentinel-1 SAR observations. *Water*, *9*(6), 366.

67. Potin, P., Rosich, B., Grimont, P., Miranda, N., Shurmer, I., O'Connell, A., Torres, R., & Krassenburg, M. (2016). Sentinel-1 mission status. *Proceedings of EUSAR 2016: 11th European Conference on Synthetic Aperture Radar*, 1–6.

68. Prasad, N. R., Garg, V., & Thakur, P. K. (2018). Role of sar data in water body mapp/ing and reservoir sedimentation assessment. *ISPRS Annals of the Photogra0/mmetry, Remote Sensing and Spatial Information Sciences*, *4*(5), 151–158. https://doi.org/10.5194/isprs-annals-IV-5-151-2018.

69. Rathore, D.S., Choudhary, A. and Agarwal, P.K. "Assessment of Sedimentation in Harakud Reservoir using digital remote sensing technique", Journal of the Indian Society of Remote Sensing, Vol.34, No.4, pp. 377-383, 2006.

70. Renwick, W.H., Carlson, K.J. and Hayes-Bohanan, J.K. "Trends in recent reservoir sedimentation rates in Southwestern Ohio", Journal of Soil and Water Conservation, Vol.60, No.2, pp. 72-79, 2005.

71. Robert, D. A., Gardener, M., Church, R., Ustin, S., Scheer, G. and Green, R. O. "Mapping Chaparral in the Santa Monica Mountains using Multiple End member Spectral Mixture Analysis", Remote Sensing of Environment, Vol. 65, pp. 267-279, 1998.

72. Roberts, D. A., Smith, M. O., and Adams, J. B. "Green vegetation, non-photosynthetic vegetation, and soils in AVIRIS data", Remote Sensing of Environment, Vol. 44, pp. 255–269, 1993.

73. Rodrigo Sagardia. "Use of Sub-pixel classifier for wetland mapping", A case study of Cuitzeo Lake Mexico, 2005.

74. Ruescas, B.A., Sobrino, A.J., Yves Julien, J.C., Jiménez-Muñoz, Guillem Sòria, Victoria Hidalgo, Mariam Atitar, Belen Franch, Juan Cuenca and Cristian Mattar, "Mapping sub-pixel burnt percentage using AVHRR data. Application to the Alcalaten area in Spain", International Journal of Remote Sensing, Vol. 31, No. 20, pp. 5315-5330. 2010.

75. Schumann, G. J. P., & Moller, D. K. (2015). Microwave remote sensing of flood inundation. *Physics and Chemistry of the Earth*, *83–84*, 84–95. https://doi.org/10.1016/j.pce.2015.05.002.

76. Settle, J.J. and Drake, N.A. "Linear mixing and the estimation of ground cover proportions. International Journal of Remote Sensing", Vol. 14, No.6, pp. 1159-1177,1993.

77. Shimabukuro, Y. E., and Novo, E.M. “Identification and mapping of the Amazon habitats using a mixing model”, International Journal of Remote Sensing, Vol. 18, No. 3, pp.663-670, 1997.

78. Silván-Cárdenas, J.L. and Wang, L. “Retrieval of subpixel Tamarix canopy cover from Landsat data along the Forgotten River using linear and nonlinear spectral mixture models”, Remote Sensing of Environment, Vol. 114, No. 8, pp. 1777-1790, 2010.

79. Simic Anita, Jing. M.C., Jane Liu, and Ferko Csillag. “Spatial scaling of net primary productivity using subpixel information”, Remote Sensing of Environment, Vol. 93, pp. 246-258, 2004.

80. Smith, L.C., and Pavelsky, T.M. “Remote sensing of volumetric storage changes in lakes”, Earth Surface Process and Landforms, Vol. 34, pp. 1353-1358, 2009.

81. SNAP Software, Help Document 2019. Available online: https://step.esa.int/main/toolboxes/snap.

82. Tatem, A. J., Lewis, H. G., Atkinson, P. M., & Nixon, M. S. (2002). Super-resolution landcover pattern prediction using a Hopfield neural network. Remote Sensing of Environment, 9, 1–14.

83. Tompkins, S., Mustard, J.F., Pieters, C.M., and Forsyth, D.W. “Optimization of endmembers for spectral mixture analysis”, Remote Sensing of Environment, Vol. 59, pp.492-489, 1997.

84. Twele, A., Cao, W., Plank, S., & Martinis, S. (2016). Sentinel-1-based flood mapping: a fully automated processing chain. *International Journal of Remote Sensing*, *37*(13), 2990–3004.

85. Van der Meer, F. “Spectral Unmixing of Landsat Thematic Mapper data”, International Journal of Remote Sensing, Vol. l6, No. 16, pp. 3189- 3194, 1995.

86. Vibulsresth, Srisangthong, D., Thisayakorn, K., Suwanwerakamtorn, R., Wongpam, S., Rodpram, C, Leelitharn, S. and Jiltanaon, W. “The reservoir capacity of Ubolratana dam between 173 and 180 meters above mean sea level”, Asian-Pacific Remote Sensing Journal, Vol. 1 No.1, pp. 1-10, 1988.

87. Weng Qihao, and Lu Dengsheng, “A sub-pixel analysis of urbanization effect on land surface temperature and its interplay with impervious surface and vegetation coverage in Indianapolis, United States”, International Journal of Applied Earth Observation and Geoinformation, Vol.10, pp.68-83, 2008.